NASA Technical Memorandum 106394
ICOMP–93–45

Head-On Collision of Drops – A Numerical Investigation

M.R. Nobari and Y.-J. Jan
The University of Michigan
Ann Arbor, Michigan

and

G. Tryggvason
Institute for Computational Mechanics in Propulsion
Lewis Research Center
Cleveland, Ohio

and *The University of Michigan*
Ann Arbor, Michigan

November 1993

NASA

HEAD-ON COLLISION OF DROPS—A NUMERICAL INVESTIGATION

M.R. Nobari, Y.-J. Jan
The University of Michigan
Department of Mechanical Engineering
Ann Arbor, MI 48109

G. Tryggvason
Institute for Computational Mechanics in Propulsion
Lewis Research Center
Cleveland, OH 44135
and
The University of Michigan
Department of Mechanical Engineering
Ann Arbor, MI 48109

ABSTRACT

The head-on collision of equal sized drops is studied by full numerical simulations. The Navier-Stokes equations are solved for the fluid motion both inside and outside the drops using a front tracking/finite difference technique. The drops are accelerated toward each other by a body force that is turned off before the drops collide. When the drops collide, the fluid between them is pushed outward leaving a thin layer bounded by the drop surface. This layer gets progressively thinner as the drops continue to deform and in several of our calculations we artificially remove this double layer once it is thin enough, thus modeling rupture. If no rupture takes place, the drops always rebound, but if the film is ruptured the drops may coalesce permanently or coalesce temporarily and then split again.

I. INTRODUCTION

The dynamics of fluid drops is of considerable importance in a number of engineering applications and natural processes. The combustion of fuel sprays, spray painting, various coating processes, as well as rain are only a few of the more common examples. While it is often possible to focus attention on the dynamic of a single drop and how it interacts with the surrounding flow, it is necessary to account for the interactions

between the drops and their collective effect on the flow when the number of drops per unit volume is high. The collision of two drops is an extreme case of two drop interaction and has been the topic of several investigations. The collision process generally involves large deformations and rupture of the interface separating the drops, and has not been amenable to detailed theoretical analysis. Previous studies are therefore mostly experimental, but sometimes supplemented by greatly simplified theoretical argument. Here, we present numerical simulations of the head-on collision of two drops, where the full Navier-Stokes equations are solved to give a detailed picture of the flow during collision.

Previous investigations of droplet collision have been motivated by raindrop formation (Brazier-Smith, Jennings and Latham, 1972; Spengler and Gokhale, 1973, and others), by efforts to predict the phase distribution in agitated liquid-liquid dispersions (Park and Blair, 1975), by concern about blade erosion due to dispersed liquid drops in low pressure turbines (Ryley and Bennett-Cowell, 1967) and by fuel spray behavior (Ashgriz and Givi, 1987). Recent experimental studies include those of Azhgriz and Poo (1990), and Jiang, Umemura and Law (1992) who show several sequences of photographs of the various mode of collision for both water and hydrocarbon drop. Drop collisions can generally be classified into four main categories: bouncing collision, where the drops collide and separate, retaining their identity; coalescence collision, where two drops become one; separation collision, where the drops temporarily become one but then break up again; and shattering collision, where the impact is so strong that the drops break up into several smaller drops. The form of the collision depends on the size of the drops, their relative velocities and the physical properties of the fluids involved. In addition to head-on collisions, off-centered collisions (where the drops are displaced radially with respect to each other) is discussed by both Azhgriz and Poo and Jiang *et al.* Other investigations may be found in Bradley and Stow (1978), Podvysotsky and Shraiber (1984) and Ashgriz and Givi (1987), for example. The major goal of these investigations has been to clarify the boundaries between the major collision categories and explain how they depend on the properties of the problem. As the large differences between water drops and hydrocarbon drops, studied by Jiang *et al.*, show, even the relatively simple case of head on collisions of equal size drops is still not fully understood.

Previous theoretical investigations of drop behavior have almost all been concerned with the oscillations of a single drop. The linear oscillations of inviscid drops are well understood (see e.g. Lamb, 1932) and several authors have looked at nonlinear effects. Recent work includes analysis by Tsamopoulos and Brown (1983) and computations by Patzek, Benner, Basaran and Scriven (1991). The decay of linear oscillations due

to viscosity was analyzed in an approximate way by Lamb (1932) in the limit of small viscosity and a more detailed analysis was later carried out by Reid (1960), Miller and Scriven (1968) and others. Numerical investigations of viscous effects can be found in Foote (1973) who used the Marker And Cell (MAC) method to solve the full Navier Stokes equations, and Mansure and Lundgren (1988) who used a boundary integral method, modified to account for small viscous dissipation in an approximate way.

The only simulation of drop collision that we are aware of is by Foote (1975) who followed the evolution of rebounding drops at low Reynolds and Weber number using the MAC method. The shapes computed by Foote have been compared with experimental observations by Bradley and Stow (1978) who found good agreement, but made the interesting observation that "this complicated treatment gives little insight into the physical processes involved." Our simulations extend the work of Foote, increasing the Weber number and exploring what happens when the drops coalesce.

The rest of the paper is laid out as follows: In section 2 we discuss briefly the numerical method which has been described in more detail elsewhere. Section 3 contains our results and section 4 is devoted to discussions. In section 5 we summarize our results. Preliminary results have been presented at the 45 Annual Meeting of the Fluid Dynamics Division of the American Physical Society (Nobari and Tryggvason, 1992).

II. FORMULATION AND NUMERICAL METHOD

The numerical technique used for the simulations presented in this paper is a front tracking method for multi-fluid flows developed by Unverdi (1990) and discussed by Unverdi and Tryggvason (1992 a,b). The actual code is an axisymmetric version of the method, described in Jan and Tryggvason (1993). Here we only briefly outline the procedure.

The physical problem and the computational domain is sketched in Figure 1. The domain is axisymmetric and the drops are initially placed near each end of the domain. A force is applied to the drops to drive them together and turned off before the drops collide. Generally, the density and viscosity of the ambient fluid are much smaller than of the drop fluid and thus have only a small effect on the results. While it is therefore sufficient to solve only for the fluid motion inside the drop, here we solve for the motion everywhere, both inside and outside the drops. The Navier-Stokes equations are valid for both fluids, and a single set of equations can be written for the whole domain as long as the jump in viscosity and density is correctly accounted

for and surface tension is included. In component form these equations are

$$\frac{\partial \rho v_r}{\partial t}+\frac{1}{r}\frac{\partial}{\partial r}r\rho v_r^2+\frac{\partial}{\partial z}\rho v_z v_r = -\frac{\partial p}{\partial r}+\frac{\partial}{\partial r}2\mu\frac{\partial v_r}{\partial r}+2\mu\frac{\partial}{\partial r}\Big(\frac{v_r}{r}\Big)+\frac{\partial}{\partial z}\mu\Big(\frac{\partial v_z}{\partial r}+\frac{\partial v_r}{\partial z}\Big)+\delta(F_s)_r$$

$$\frac{\partial \rho v_z}{\partial t}+\frac{1}{r}\frac{\partial}{\partial r}r\rho v_r v_z+\frac{\partial}{\partial z}\rho v_z^2 = -\frac{\partial p}{\partial z}+\frac{1}{r}\frac{\partial}{\partial r}\mu r\Big(\frac{\partial v_z}{\partial r}+\frac{\partial v_r}{\partial z}\Big)+\frac{\partial}{\partial z}2\mu\frac{\partial v_z}{\partial z}+\delta(F_s)_z+f_z$$

Here, v_z and v_r are the velocity components in the axial and radial direction, p is the pressure, and ρ and μ are the discontinuous density and viscosity fields, respectively. F_s is the surface tension force and f_z is a body force. Notice that the surface tension force has been added as a delta function, only affecting the equations where the interface is. The detailed form of F_s will be discussed below. The above equations are supplemented by the incompressibility conditions

$$\frac{1}{r}\frac{\partial}{\partial r}rv_r+\frac{\partial}{\partial z}v_z = 0$$

which, when combined with the momentum equations leads to a non-separable elliptic equation for the pressure, and equations of state for the density and viscosity:

$$\frac{\partial \rho}{\partial t}+\mathbf{u}\cdot\nabla\rho = 0; \quad \frac{\partial \rho}{\partial t}+\mathbf{u}\cdot\nabla\mu = 0.$$

These last two equations simply state that density and viscosity within each fluid remains constant.

Nondimensionalization gives a Weber and a Reynolds number defined by:

$$We = \frac{\rho_d d U^2}{\sigma}; \qquad Re = \frac{\rho_d U d}{\mu_d}.$$

In addition, the density ratio ρ_o/ρ_d and the viscosity ratio μ_o/μ_d must be specified. Here, d is the drop diameter. The subscript d denotes the drop fluid and o the ambient fluid. When presenting our results we scale lengths by the initial diameter of the spherical drop and velocity by $V = U/2$, the speed of one drop before impact. To nondimensionalize time we have the choice of two inherent time scales: One is the advection time d/V of the drops before impact and the other is the natural oscillation time for the drop $\tau_d = (\pi/4)\sqrt{\rho d^3/\sigma}$. While most of our results are presented using the advective time scale, in some cases the latter is the more natural one (as pointed out already by Foote, 1975). In a few cases we therefore replot our results using this time scale.

The force used to drive the drops together initially is taken as

$$f_z = A(\rho - \rho_o)\text{sign}(z - z_c)$$

so the force acts only on the drops. Here A is an adjustable constant and z_c is midway between the drops. This force is turned off before the actual collision takes place. In most of our simulations the drops are initially put about one diameter apart (two diameters between their centers) and A is varied to give different collision velocities. To make comparison between various runs easier, we set time equal to zero when the centers of the drops are one diameter apart. If the drops were exactly spherical, they would touch at this instant. In our case, since the drops are moving in an other fluid, they have generally deformed slightly before impact and there is therefore a layer of ambient fluid between them at this time.

To solve the Navier-Stokes equations we use a fixed, regular, staggered grid and discretize the momentum equations using a conservative, second order centered difference scheme for the spatial variables and an explicit first order time integration method. We have used second order time integration in other problems and generally find little differences for relatively short simulations times as those of interest here. The effect does show up in long time simulations and is usually accompanied by a failure to conserve mass. In the computations discussed here, mass is always conserved within a fraction of a percent. The interface is represented by separate computational points that are moved by interpolating their velocity from the grid. These points are connected to form a front that is used to keep the density and viscosity stratification sharp and to calculate surface tension forces. At each time step information must be passed between the front and the stationary grid. This is done by a method that has become known as the Immersed Boundary Method and is based on assigning the information carried by the front to the nearest gridpoints. While this replaces the sharp interface by a slightly smoother grid interface, all numerical diffusion is eliminated since the grid-field is reconstructed at each step.

The original Immersed Boundary Method was developed by Peskin and collaborators (see e.g. Peskin 1977) for homogeneous flows. The extension to multi-fluid flows includes a number of additional complications. The first is that density now depends on the position of the interface and has to be updated at each time step. There are several ways to do this but we use a variant of the method developed by Unverdi (1990) where the density jump at the interface is distributed onto the fixed grid to generate a grid-density-gradient field. The divergence of this field is equal to the Laplacian of the density field and the resulting Poisson equation can be solved efficiently by a Fast Poisson Solver. The particular attraction of this methods is that close interfaces can interact in a very natural way, since the grid-density-gradients

simply cancel. Therefore, when two interfaces come close together the full influence of the surface tension forces from both interfaces is included in the momentum equations, but the mass of the fluids in the thin layer between the interfaces—which is very small—is neglected. A second complication is that the pressure equation now has a nonconstant coefficient (or is non-separable) since the density varies. This prevents the use of Fast Poisson Solvers based on Fourier Methods, or variants there of, and we have used a multigrid package, MUDPACK, from NCAR (see Adams, 1989, for a description) with slight modifications due to our staggered grid.

The computation of the surface tension forces poses yet another difficulty. Generally, curvature is very sensitive to minor irregularity in the interface shape and it is difficult to achieve accuracy and robustness at the same time. However, by computing the surface tension forces directly by

$$\mathbf{F}_s = \sigma \int_{\Delta s} \frac{\partial \mathbf{s}}{\partial s} ds,$$

where $\mathbf{s}$ is the tangent vector, we ensure that the net surface tension force is zero, or:

$$\oint \sigma \kappa \mathbf{n} da = 0.$$

Here, $\mathbf{n}$ is the outward normal and κ is the mean curvature. This is important for long time simulations since even small errors can lead to a net force that moves the drop in an unphysical way.

Lastly, contrary to previous computations with the Immersed Boundary Method, the interface deformes greatly in our simulations and it is necessary to add and delete computational elements during the course of the calculations. While this is a major task for fully three-dimensional simulations, here the interface is simply a line and such modifications are a simple matter.

The method and the code has been tested in various ways, such as by extensive grid refinement studies, comparison with other published work and analytical solutions (for details see Jan, 1993 and Nobari, 1993). Generally, both analytical solutions and other simulations are limited to relatively simple cases. We include one test in figure 2 where we compare the oscillations of a single drop with analytical predictions. Here a single drop is perturbed slightly by the fundamental mode. The drop oscillates and the amplitude of the fundamental mode is plotted in the figure. The oscillation period is close to what is predicted by Lamb (formula number 10 on page 475) with $t_{\text{compute}}/\tau_d = 1.03$, and the decay compares also well with formula 12 on page 641 in Lamb. The envelope for the oscillations, as computed by Lamb's equation is plotted in figure 2. We have compared several cases and find, as expected, that as the

perturbation amplitude and the viscosity becomes smaller, fully resolved simulations give results in close agreement with the theoretical predictions. For large amplitude perturbations, the oscillation frequency is also well predicted by Lamb's formula, if the diameter of a sphere of the same volume as the drop is used.

III. RESULTS

We have computed a large number of collisions and in this section we show several results. First we consider collisions where the interface between the drops is not ruptured, and then we discuss collisions with interface rupturing.

A. Bouncing drops

Figure 3 shows the collision of two drops, at several times. Here, $We = 32$, $Re = 98$, $\rho_d/\rho_o = 15$, and $\mu_d/\mu_o = 350$. Initially, a constant force acts on the drops to accelerate them toward each other. When the drops are about half a diameter apart, the force is turned off, but the drops have acquired enough momentum to continue toward each other and collide. As the drops come in contact, the fluid between them is squeezed away and the drops bulge out at the equator of the combined fluid mass. The bulk of the fluid continues to move forward and then outward to the rim of the drop—which is now more disk-like—thus resulting in an indentation in the middle. Surface tension eventually inhibits further outward motion of the rim and forces the fluid back toward the axis of symmetry. While kinetic energy is converted into surface tension energy during the initial deformation, the reversed motion converts surface tension energy back into kinetic energy and the drops rebound since the interface between the drops is not allowed to rupture.

This calculation was done on a uniform grid with 64 by 256 meshes in the radial and axial direction, respectively. To show that this is an essentially fully converged solution we compare selected frames from the run in figure 3 with computations done on a coarser, 32 by 128, grid in figure 4. The most significant difference is that the coarsely resolved drops have moved slightly less apart than the well resolved ones, suggesting slightly larger loss of energy for low resolution. For all our simulations we have monitored the volume conservation of the drops (not explicitly enforced in the code) and found that even for collisions involving severe deformations the volume change is always less than a fraction of a percent.

In figure 5 we show the time evolution of various quantities for the run in figure 3. In (a) and (b) we show the position of the center of mass for the drop and the velocity of the center of mass, respectively. For reference, a horizontal line is drawn one

drop radius from the symmetry plane in (a), and if the drops remained spherical they would not touch once the center of mass is above this line. In reality the drops deform slightly before colliding and elongate after collision. The drops are set in motion by a constant force and the velocity in (b) therefore increases linearly. Once the force is turned off, the drops slow down slightly due to the drag from the surrounding fluid, and after collision the drops return to a steady motion with a velocity that is about half of their velocity before collision.

In 5(c) we plot the nondimensional maximum diameter of the drop, and its deformation, defined as the ratio of maximum diameter divided by the thickness of the drop on the symmetry axis. While the drops are squashed together during the collision, they are elongated during rebounding. Notice that the radius does not start to increase until well into the collision and that the deformation curve is not symmetric about its peak, illustrating that the initial squashing is considerably slower than the subsequent recovery. The energy balance during the collision is shown in figure 5(d) where the kinetic energy of the drop and the surface tension energy, along with the total energy of the drop, is plotted versus time. Initially, only the kinetic energy increases as the drops are set in motion by the applied force field. When the force field is turned off, the energy decreases slightly due to viscous dissipation. During the collision the kinetic energy is converted into surface tension energy, which reaches maximum at the maximum drop deformation when the kinetic energy is nearly zero. Notice the rapid decay in the total energy during the initial stage of the collision when the drops become flatter; the "pause" in the dissipation at maximum deformation, and again the rapid dissipation when the drops recover their spherical shape. In the particular case shown here, the total energy dissipation is divided unequally between the initial deformation phase and the recovery phase, with larger dissipation taking place during the recovery stage. After the drops rebound, the surface and kinetic energy curves are slightly wavy, due to the oscillations of the drops and the total energy decreases at a rate comparable with the decay before collision. Comparing 5 (a), (b), (c), and (d) we see that the maximum surface energy coincides with zero centroid velocity, but the maximum deformation occurs slightly later since the drops continue to become thinner in the center, even after the outward motion has stopped.

Drops colliding with solid surfaces can cause extensive damage, and since the drops in figure 3 are of the same size, they behave as a drop colliding with a non-wetting, full-slip surface. Although real surfaces are not full-slip, it is likely that the differences are small at high Reynolds numbers. Figure 5e shows the force on the symmetry plane computed by integrating the pressure over the area where the drops touch. Notice that the maximum force coincides with the point where the centers of

mass are closest and that the maximum force is more than twice the average force. We have also estimated the average force by dividing the impulse needed to change the momentum of the drop by the collision time and find good agreement.

To get additional insight into the collision process, we plot the velocity vectors inside the drop, as well as the streamlines for the whole flow field, at several times, in figure 6. The velocity vectors are to the right and (the mirror image of) the streamlines on the left. In the first frame the drops have collided and while the fluid in most of the drop is still moving forward with uniform velocity, the fluid in a small region near the collision plane, is moving outward. The forward motion of the drops has induced a circulation in the whole fluid domain leading to closed streamlines. In the outer fluid, near the drop surface there is a thin shear, visible as a "kink" in the streamlines. In the next frame, the region where the velocity is uniform and the streamlines are straight has nearly disappeared as more and more of the fluid is squeezed outward. Near the rim of the resulting disk the outward velocity eventually goes to zero, and in the third frame the outer rim is starting to flow inward, even though the middle of the disk is still getting thinner (the droplet never becomes completely stationary, thus the kinetic energy is never exactly zero). This reversed flow region continues to grow and in the fourth frame the flow is dominated by a large recirculation region of opposite circulation to the initial one. This development continues in the next two frames as the drops rebound. Since the flow near the walls of the domain is now toward the collision plane, a small reminder of the fluid with the original circulation accumulates near the outer walls. Notice that the flow field during recovery is not simply the reverse of the initial flow. While the drop was getting flatter, considerable amount of the drop fluid remained in uniform motion during a large fraction of the collision phase; during recovery the streamlines bend more uniformly.

The pressure field inside the drops, at the same times as in figure 6, is plotted in figure 7. Because of finite resolution, the pressure is not exactly discontinuous across the interface, but changes smoothly over two to three grid spaces. For relatively fine resolution, as is the case here, this transition zone is thin. Initially, the pressure is nearly uniform within the drops, but as the drops collide and are brought to a halt, the pressure on the centerline, at the point of contact, increases. As the contact region increases the high pressure area moves to the rim of the disc, and at maximum deformation, when the drop is nearly stationary, the pressure is highest in the outer torus, where the curvature is highest. This high pressure drives the flow back during rebounding and as the drops separate the high pressure region is again on the contact plane. Here the drops are elongated during separation and the pressure is therefore highest near the ends where the curvature is highest. Notice that the vertical scale

in each frame is different.

In laboratory experiments, bouncing is actually rather rare and drops generally coalesce when the film between them ruptures. The time of rupture depends on how fast fluid is drained out of the film and while we do not attempt to resolve the thin film, the computations give information that could be used to predict the drainage time. ¿From figure 3 and 4, it is clear that the area where the drops are in contact (separated only by a thin film) is well defined and not sensitive to the resolution. In figure 8a, we plot the radial position of the outer edge of this area versus time. In figure 8b we plot the pressure in the symmetry plane versus radius at several times. The earliest line, at t=0.2, corresponds to the second frame in figure 7. Here, the pressure is nearly uniform across the line of contact. As the drops become flatter the pressure on the centerline falls rapidly, but the pressure near the rim of the disk increases. This high pressure near the rim eventually forces the fluid back, again increasing the centerline pressure. As the drops rebound the centerline pressure becomes nearly uniform over the plane of contact and decreases. The radial velocity in the symmetry plane is plotted in figure 8c for the same times as in figure 8b. Initially, the velocity is nearly a linear function of radius, but then the fluid near the rim slows down and starts to flow back while the velocity near the center is still positive. Near the end of the collision, the velocities are again nearly linear, but now in the inward direction. This velocity is taken directly from the simulations in figure 3 and since the film is many times smaller than the grid spacing, this velocity is not affected by the properties of the film fluid. If the radial velocity in the film was different, one would expect a boundary layer inside the drop to match this velocity.

Experimental observation suggest that the effect of the Reynolds number is small, once it is high enough. Although our Reynolds numbers are somewhat lower than those often encountered experimentally, we find a similar trend. In figure 9 we compare the results for a single Weber number and three Reynolds numbers. (The case shown in figure 3 has the same Weber number and is also included in the comparisons made in figure 10 and 11.) Except for the very lowest Re, the solutions are quite similar. A more detailed comparison is given in figure 10 where the energies are plotted versus time. (Since the Weber numbers are not exactly identical, the curves do not coincide completely at time zero.) In all cases, the kinetic energy is reduced at nearly the same rate, but the rate of increase in surface tension energy is the same only for the two highest Reynolds numbers. The difference is due to dissipation as seen in the graph for the total energy. When the drops bounce back, the rate of recovery of kinetic energy is different for all Reynolds numbers, although the difference is the smallest for the highest Reynolds numbers. Notice that for the highest

Reynolds numbers more energy is dissipated during the rebounding stage than during the initial impact. This is also seen in Figure 11a where the energy loss during initial impact (up to the maximum deformation) and the total energy loss are compared for the different Reynolds numbers. In figure 11b the maximum radius and the maximum deformation are plotted versus Reynolds number. While the maximum radius is relatively independent of Reynolds number once it is high enough, the deformation continues to increase. Overall, the collision becomes relatively independent of Reynolds number for the highest values simulated and this is also reflected by the coefficient of restitution which is plotted in figure 11c. The restitution coefficient and the energy loss are computed when the distance between the drop center of mass is one diameter, since there is a small energy dissipation after the drops separate due to friction from the outer fluid.

With collision at high Reynolds numbers becoming relatively independent of Reynolds number, the Weber number remains the main controlling parameter. Its influence on the collisions is examined in figure 12 where the drops are shown at several times for three different Weber numbers. In the top row the Weber number is smaller than in the computations in figure 3 and 4, but in the two lower rows the Weber numbers are larger. There are obviously considerable differences. For the lowest Weber number the drops deform only slightly during the collision and return to nearly spherical shape immediately following separation. As the Weber number is increased the deformation increases considerably and the drops become greatly elongated as they separate. The time here is scaled by the initial velocity and on this timescale the collision takes longer for the higher Weber numbers. We have run the code at higher Weber numbers, but generally found it difficult to follow the computations throughout a complete bouncing due to instabilities in the thin film near the centerline. Whether this is a resolution problem or due to a physical instability has not been resolved. The question is most likely of marginal physical relevance since very thin films are likely to rupture for these high Weber numbers.

The velocity of the center of mass is plotted in figure 13a. For the lowest Weber numbers the velocity changes smoothly from positive to negative, indicating a nearly constant deceleration of the center of mass. As the Weber number increases, the velocity decreases more rapidly, but the curve develops a kink at the point of maximum deformation, where the velocity of the center of mass remains essentially zero as the drops become flatter. This "waiting" becomes longer as the Weber number increases and the final velocity of the drops after rebounding decreases due to the larger dissipation in the more deformed drops. The time in figure 13a is scaled using the velocity of the drops before collision. In figure 13b the time has been rescaled by

the oscillation frequency of the drop and in this units the total collision time is nearly constant!

Figure 14 shows the force on the symmetry plane versus time. As the Weber number increases, the drops become "softer" and the maximum lower. For the lowest Weber number the force has a single maximum, but for the higher Weber numbers there is a large maximum at the initial impact and another smaller one as the drops recover their shape and bounce back. The average force also decreases since the contact time increases and the net change of momentum during the collision becomes smaller since the final velocities are lower due to larger dissipation for larger deformation.

In figure 15 we examine the energies as a function of time for the runs in figure 12 using time units based on the oscillation frequency of a single drop (as in figure 13b). As the drops collide the kinetic energy (figure 15a) is reduced to nearly zero for all cases but the amount recovered depends strongly on the Weber number, with most energy dissipated for high Weber numbers where the deformations are large. This figure shows, as did figure 13b, that in the time units used here the time of collision is relatively constant for the higher Weber numbers. Furthermore, the post collision oscillations have nearly the same period—as expected. The surface tension energy, shown in figure 15b, actually has a smaller maximum for the higher Weber numbers, even though deformation is much larger, due to the increased dissipation. The total energy is shown in 15c. Here, it is obvious that the difference in energy losses is mostly due to different dissipation during the initial deformation.

Figure 16 summarizes the results for different Weber numbers: As the Weber number increases, the drops deform more and the energy losses increase (16a), with nearly all the initial kinetic energy being dissipated at the highest We. The initial losses, up to maximum deformation, are about a third of the total losses for low We and increase to about half the losses for high We. As the deformation and energy dissipation increases, the restitution coefficient (16b) and the average collision force (16c) decrease. The collision time (16d), as measured in units based on the oscillation period of a single drop—and defined as the time from when the drops would first touch if they remained spherical until the time when the drops actually separate—decreases slightly at low Weber numbers and then remains relatively constant at higher We. This remarkable simple dependency of the collision time on We has been observed before (see e.g. Foote, 1975). For bouncing drops the collision time is, of course, of a critical importance, since it influences not only the total force exerted by the drop, but may also be important for mass and heat transfer. Furthermore, for coalescence to take place it is necessary that the collision takes sufficiently long time so that fluid can be drained from the film separating the drops. Translated into dimensional

variables, constant $t_{\text{collision}}/\tau_d$ means, for example, that for a given fluid and drops size the collision time does not depend on the velocity of the drops. Low impact velocities (low We) will lead to small deformations, and large velocities (high We) to large deformations but the time in contact is the same. However, for the same fluids and same impact velocities, larger drops will have a longer contact time. Similarly, for the same size and impact velocities, drops with higher surface tension will bounce off each other faster than low surface tension drops.

B. Coalescing drops

In the above computations we have not ruptured the layer between the drops and therefore the drops can never coalesce. Real drops, however, generally coalesce (bouncing is actually somewhat rare) and the interface has to be ruptured for simulations of realistic collisions. Thin films usually rupture when their thickness becomes comparable with the intermolecular spacing (about 100-400 Angstrom, see, for example, Bradley and Stow 1978). We can not resolve the layer down to such a small scale, although the computations in figure 3-5 suggest that the large scale motion is well predicted and—in particular, and perhaps somewhat surprisingly—does not depend on the resolution of the layer. When the layer ruptures, however, the resulting change in the interface topology usually leads to dramatically different evolution from when the layer is not ruptured. The theory of film rupture between bubbles or drops is currently being developed (see e.g. Davis et al, 1989, and Yiantsios and Davis, 1991), and while it appears possible that such a theory can be combined with full simulations, we take a more *ad hoc* approach here and rupture the interface at a prescribed time by removing surfaces which are very close. Such instantaneous change in topology is, of course, an approximation to what happens in reality. While the influence of molecular forces, where the actual rupture takes place, is confined to a small area, there generally follows an extremely rapid motion of the surrounding film where surface tension forces pull the remaining sheets and filament together, often leading to further rupture and the formation of small droplets. We ignore these rapid small scale processes entirely, also throwing away any small isolated drops that may be formed following the rupture. Modeling the rupture by a discontinuous change in the structure of the interface is therefore a little like modeling a shock wave by a discontinuity. Although this "shock" is in time, rather than space, the analogy is made even more appropriate by the fact that usually the topology change is accompanied by a loss of surface and total energy.

In figure 17 we show the same collision as in figure 3 and 4 where the interface is ruptured once the drops are close enough. In (a) the film is ruptured at time

0.4 by simply removing the double interface, leaving a single drop with indented waist. Surface tension pulls this indentation outward initially, but after the drop has reached its maximum deformation, surface tension pulls the waist inward and the drop elongates before starting to oscillate around the spherical equilibrium shape. The sensitivity of the evolution to the exact instance of rupture can be seen by comparing the frames in (a) to the frames in (b) where the interface is ruptured at a later time. The evolution is comparable to the previous case, but the maximum deformation is smaller. Figure 18 shows the evolution of the energies for the runs in figure 17, as well as the run in figure 3 when no rupturing takes place. As the interface is ruptured, considerable surface area disappears and there is therefore a discontinuous reduction in the surface energy (as well as the total energy). In reality this energy is dissipated when the ruptured film breaks into small drops or is stored as surface energy of these small drops, but here the film is simply removed. The kinetic energy is, of course, unchanged by the rupture, but its subsequent evolution is different than in the non-rupturing case. Notice that in (b) there is a larger energy loss and that the post-coalescence oscillations are smaller than in (a).

We have repeated the computations in figure 12, where the Reynolds number is held constant (Re=100) and the Weber number varied, and ruptured the film between the drops at a predetermined nondimensional time (t=0.2). This early time was selected to minimize energy losses due to coalescence and since a well defined layer had formed at this stage so that removing it did not alter the total volume of the drop by any significant amount. For the We numbers simulated (up to 100) the drops coalesce permanently and figure 19a compares the maximum radius for these cases to the results where the drops bounce. When coalescence takes place, the maximum radius is larger. However, since some energy is lost when the thin film is removed, the maximum surface energy (19b) is smaller than for bouncing drops.

Another simulation, for more energetic drops (Re=140, We=65) is shown in figure 20 where we show the evolution following rupture for two different rupture times. In all cases the drops continue to become flatter, followed by a recovery that leads to a large elongation of the drop. For the first case where rupture is at an early time this elongation leads to a break up of the drop into two drops, but when the rupture is later this break up does not take place. In figure 21, the energies are plotted versus time. As the film is ruptured, there is a drop in surface energy and therefore total energy. Surface energy drops slightly following the rupture as the cusp left by the rupture is pulled back. The rate of decrease of kinetic energy is slowed, but not reversed, suggesting that considerable dissipation is taking place. As the combined drop continues to deform, surface energy increases again, reaching maximum where

the kinetic energy is minimum. Notice that the maximum is considerably later than when the interface is not ruptured. When the interface is ruptured earlier, the loss in energy is smaller, the maximum kinetic energy when the drop recovers its spherical shape is larger and subsequently, the surface energy at late time, when the kinetic energy has become nearly zero is slightly larger. This suggests that if the drops are allowed to coalesce earlier, a secondary separation will take place more easily.

We have also conducted a few simulations at even higher Reynolds and Weber number. Figure 22 shows the evolution of the interface for Re=185 and We=115 where the interface is ruptures at t=0.2. After coalescence and the initial formation of a flat "disk" the drops stretch apart, forming a chain of three nearly equal sized drops. Here, we have removed the filament connecting the drops after stretching, thus again modeled rupture. The size of the middle drop is considerably larger here than in figure 20. In experiments, several drops are often formed for more energetic collisions.

IV. DISCUSSION

In the modeling of droplet collisions the most basic question is what type of collision will result for a given set of external parameters. Most models proposed in the literature therefore try to predict the boundaries between the various collision modes. The simulations in the preceding section give detailed information about both the drop shape and the velocity field as a function of time and can help to validate the various hypotheses made in the construction of simple models.

Both Ashgriz and Poo (1990) and Jiang *et al* (1992) present simple energy arguments to explain the outcome of drop collisions. The basic difference between these models is that Ashgriz and Poo neglect dissipative effects whereas Jiang *et al* include dissipation during deformation. For drops that coalesce, Jiang *et al* (1992) argue that the dissipation up to maximum deformation is independent of the viscosity of the fluid and that most of it takes place in a thin layer near the contact plane between the drops.

¿From figure 10 and 11 we see that while the collision becomes relatively independent of the Reynolds number as Re increases, the energy dissipation does not go to zero. Indeed, there seems to be some support for the assertion that the energy loss (particularly during the initial deformation) becomes independent of the Reynolds number. To examine this in a more detail, we plot the dissipation per unit volume

$$\phi = \frac{1}{\mathrm{Re}}\left\{2\left[\left(\frac{\partial v_r}{\partial r}\right)^2 + \left(\frac{v_r}{r}\right)^2 + \left(\frac{\partial v_z}{\partial z}\right)^2\right] + \left(\frac{\partial v_r}{\partial r} + \frac{\partial v_z}{\partial z}\right)^2 - \frac{2}{3}\left[\frac{1}{r}\frac{\partial}{\partial r}(r v_r) + \frac{\partial v_z}{\partial z}\right]^2\right\}$$

for selected times and three different Reynolds numbers in figure 23. The times were selected where the dissipation is high during the initial impact (t=0.2) and during rebound (t=1.2). The figure shows that the maximum dissipation does not take place in a thin layer near the stagnation point, as assumed by Jiang *et al*, but near the outer edge of the drop where the streamlines are turning outward. However, although the maximum dissipation is occurring in a different place than they assumed, the rest of their argument seems to be supported by the plot. While the contour plots for the highest Reynolds numbers, at t=0.2, are not identical, they are considerably closer to each other than to the plot for the lowest Reynolds number, thus suggesting some level of convergence. We note that this is actually a more stringent test than the argument of Jiang *et al* requires; here we are comparing the point-wise dissipation whereas their discussion is based on the integrated value. Similar trend is seen during the rebound stage (t=1.2) where the maximum dissipation takes place near the symmetry line away from the contact plane where the streamlines converge. Overall, the dissipation is not as localized as during the initial deformation and the differences between the plots for the highest Reynolds numbers are greater. Although energy dissipation during collision may become independent of Reynolds number for $Re \rightarrow \infty$, we note that for coalescing drops, any excess energy must be dissipated by oscillations and the decay thus depend on Re.

The dissipation of energy has a significant influence on the evolution of the drops after initial contact. In particular, large dissipation reduces the maximum deformation. An upper bound on the maximum surface area can be easily determined (see e.g. Jiang *et al*, 1992): Since kinetic energy is converted into surface tension energy during collision, the surface area is maximum if no energy is lost and all the initial kinetic energy is converted into surface tension energy

$$\frac{1}{2}M_d V^2 + \sigma S_o = \sigma S_{max}.$$

Here, we ignore the outer fluid completely. M_d is the mass of a single drop and S_o and S_{max} are the initial and maximum surface area, respectively. Assuming the drops to be spherical initially, and using the definition of the Weber number this can be written as

$$\frac{S_{max}}{S_o} = 1 + \frac{4\pi r^3 \rho V^2}{23\sigma 4\pi r^2} = 1 + \frac{We}{48}.$$

This line is plotted in figure 24 for both the bouncing drops in figures 12-16 and the coalescing drops in figure 19. In both cases the maximum surface area is not achieved due to dissipation of energy. Since the interface is ruptured at a constant nondimensional time based on d/V (not oscillation period, τ_d) the drops are slightly

more deformed when the film is ruptured at higher Weber numbers and the difference between bouncing and coalescing drops therefore increases with We. In addition to our numerical results, we have also plotted data from Jiang *et al* (1992) in figure 24. The dotted line is a straight line fit to their data points. Overall there is a reasonable agreement (the data is, for example, bounded by our bouncing drops), but the slope of the experimental data is somewhat different than either of our curves. We expect that this is due to differences in the time of film rupture. At low Weber number, when the velocities are low, the time it takes to drain the film is likely to be long and losses due to rupture large. At higher We the opposite appears to hold. We note also that Jiang *et al* had to estimate the surface area from measurements of the drop radius, and some of the differences could be due to inaccuracies in this estimate.

Computations at high Re and We require fine resolution and long computational time. We have therefore simulated only a few cases for reflective collisions, defined as when the drops separate following an initial coalescence. Using these few runs and experimental data from the literature we show, in figure 25, the boundaries between coalescence and reflective collisions in the Re-We plane. The crosses, that are connected by a solid line, are obtained from the data presented by Jiang *et al* (1992) and the line to the far right is from the high Reynolds number experiments of Ashgriz and Poo (1990). The circles represent our simulations. Open circles show a coalescence collision and filled circles stand for reflective collisions. In most cases the interface was ruptured at t=0.2. The experimental data does not extend to low Reynolds numbers but our numerical data suggest—as one might expect—that reflective collisions do not take place at low Reynolds numbers. Although the comparison can only be qualitative—we do not, after all, have a physical model for the rupture time—the agreement is good where we have data and the numerical results suggest a natural extension of the experimental results to low Reynolds numbers.

While the limited number of computations that we have done for reflective collisions does not allow us to draw general conclusions, the plot of the energies in figure 21 suggest a relatively simple criteria for separation following initial coalescence: Comparing the two graphs, we see that the surface tension energy during rebound exceeds that of two drops (the horizontal line) in (a) where the drops separate, but in (b) where the drops do not separate, the losses are sufficiently large so that surface tension energy does not exceed that of two isolated drops. We therefore suspect that the drops will split if the losses due to coalescence and deformation are sufficiently small, or that

$$2(\frac{1}{2}M_d V^2 + \sigma S_o) - \Phi > 2\sigma S_o$$

where S_o is the surface area of a single spherical drop and Φ is the total losses due

to both viscous dissipation and interface rupture. While the viscous losses are fully predicted by our computations, the losses due to rupture require accurate information about the time of rupture.

V. CONCLUSIONS

The computations of head-on collisions of two drops of equal size presented here are, in many ways, quite similar to those of Foote (1975) almost twenty years ago. Indeed, we have used many of the same diagnostics as those presented by Foote and been guided by his observations. We have, of course, been able to extend both the resolution of the calculations and the range of parameters examined. In particular, we have simulated much higher Weber numbers. We have also examined the effect of rupturing the interface between the drops at predetermined times and allowing coalescence. While these studies are not exhaustive and suffer from the lack of a physics based model for the rupture time, they show both that such a model is needed, and that the rest of the computations is under good control. While the details of the rupturing remain unresolved, the computations suggest that since the evolution is relatively insensitive to the resolution of the layer between the drops, the drainage process before rupture is primarily a one-way coupling in the sense that while the drop behavior affects the draining, the exact film behavior has minimal impact on the drop. The rupture time, on the other hand, is critical to the continuing evolution of the drop, and depends on how fast the film is drained. These observations suggest that a subgrid model, which takes in the pressure and velocity of the drop fluid and predicts the rupture time, which is the only information returned back to the drop simulations, would give a procedure that had a fully predictive capability. Such a subgrid model for the rupture, that is suitable for our approach, has been presented by Jacqmin and Foster (1993), but has not been incorporated into our code yet. We note that accurate prediction of the time of rupture requires careful tracking of the front and that numerical techniques that relay on grid based reconstruction of the interface (such as the Volume-of-Fluid method) are not able to predict the delay in rupture due to a finite drainage time.

The simulations presented here are only a first step in a comprehensive numerical study of droplet collisions. Both a reliable rupture model and fully three dimensional simulations will be required before a complete insight and predictive capability are in place. Both extensions appear to be within sight. The subgrid model of Jacqmin and Foster (1993) was mentioned above; preliminary three-dimensional simulations are presented by Nobari and Tryggvason (1993).

ACKNOWLEDGMENT

We would like to acknowledge discussions with Dr. D. Jacqmin at the NASA Lewis Research Center. Part of this work was done while one of the authors (GT) was visiting the Institute for Computational Mechanics in Propulsion at NASA Lewis. This work was supported by NASA grant NAG3-1317, and partly by NSF grant CTS-913214. Some of the computations were done at the San Diego Supercomputing Center which is funded by the National Science Foundation.

REFERENCES

J. Adams, "MUDPACK: Multigrid Fortran Software for the Efficient Solution of Linear Elliptic Partial Differential Equations," Applied Math. and Comput. **34**, 113 (1989).

N. Ashgriz and J.Y. Poo, "Coalescence and separation in binary collisions of liquid drops," J. Fluid Mech. **221**, 183 (1990).

N. Ashgriz and P. Givi, "Binary collision dynamics of fuel droplets," Intl. J. Heat Fluid Flow **8**, 205 (1987).

S. G. Bradley and C. D. Stow, "Collision between liquid drops," Phil. Trans. R.Soc. Lond. A **287**, 635 (1978).

P. R. Brazier-Smith, S. G. Jennings and J. Latham, "The interaction of falling water drops: coalescence," Proc. R. Soc. Lond. A **326**, 393 (1972).

R. Davis, J. Schonberg, and J. Rallison, "The lubrication force between two viscous drops," Phys. Fluids. A 1(1), 77 (1989).

G. B. Foote, "A numerical method for studying liquid drop behavior; Simple oscillations," J. Comput. Phys. **11**, 507 (1973).

G.B. Foote, "The Water Drop Rebound Problem: Dynamics of Collision," J. Atmos. Sci. **32**, 390 (1975).

D. Jacqmin and M.R. Foster, "The evolution of thin films generated by the collision of highly deforming droplets," Submitted for publication.

Y.-J. Jan and G. Tryggvason, "The rise of contaminated bubbles," In preparation.

Y.-J. Jan, *Ph.D. Thesis* (The University of Michigan, 1993).

Y. J. Jiang, A. Umemura, and C.K Law, "An experimental investigation on the collision behaviour of hydrocarbon droplets," J. Fluid Mech. **234**, 171 (1992).

H. Lamb, *Hydrodynamics* (Dover, New York, 738, 1932).

T.S. Lundgren and N.N. Mansour, "Oscillation of drops in zero gravity with weak viscous effects," J. Fluid Mech. **194**, 479 (1988).

C.A. Miller and L.E. Scriven, "The oscillation of a fluid droplet immersed in another fluid," J. Fluid Mech. **32**, 417 (1968).

M.R. Nobari, *Ph.D. Thesis* (The University of Michigan, 1993).

M.R. Nobari and G. Trygvason, "Head-on collision of drops," Bull. Amer. Phys. Soc. 37: 1972 (1992). (Abstract only)

M.R. Nobari and G. Trygvason, "Numerical simulation of three-dimentional droplet collision," In preparation

J.Y. Park and L.M. Blair. "The effect of coalescence on drop size distribution in an agitated liquid-liquid dispersion," Chem. Engng. Sci. **30**, 1057 (1975).

T.W. Patzek, R.E. Benner, O.A. Basaran, and L.E. Scriven, "Nonlinear oscillations of inviscid free drops," J. Comp. Physic. **97**, 489 (1991).

N. A. Pelekasis, J. A. Tsamopoulos and G. D. Manolis, "Equlibrium shapes and stability of charged and conducting drops," Phys. Fluid A **2**, 1328 (1990).

C. S. Peskin, "Numerical analysis of blood flow in the heart," J. Comput. Phys. **25**, 220 (1977).

A.M. Podvysotsky and A.A. Shraiber, "Coalescence and breakup of drops in two phase flows," Intl. J. Multiphase Flow **10**, 195 (1984).

W. Reid. "The oscillation of a viscous drop," Quart. Appl. Math. **18**, 86 (1960).

D.J. Ryley and B.N. Bennett-Cowell, "The collision behaviour of steam-borne water drops," Int. J. Mech. Sci. **9**, 817 (1967).

J.D. Spengler and N.R. Gokhale, "Drop Impactions," J. Appl. Meteor. **12**, 316 (1973).

J.A. Tsamopoulos and R.A. Brown, "Nonlinear oscillations of inviscid drops and bubbles," J. Fluid Mech. **127**, 519 (1983).

S. O. Unverdi, *Ph.D. Thesis* (The University of Michigan, 1990).

S. O. Unverdi and G. Tryggvason, "A Front Tracking Method for Viscous Incompressible Flows," J. Comput. Phys., **100**, 25 (1992).

S. O. Unverdi and G. Tryggvason, "Multifluid flows," Physica D **60**, 70 (1992).

S. Yiantsios and R. Davis, "Close approach and deformation of two viscous drops due to gravity and Vander Waals forces," J. Coll. Interface sci. **144**, 412 (1991).

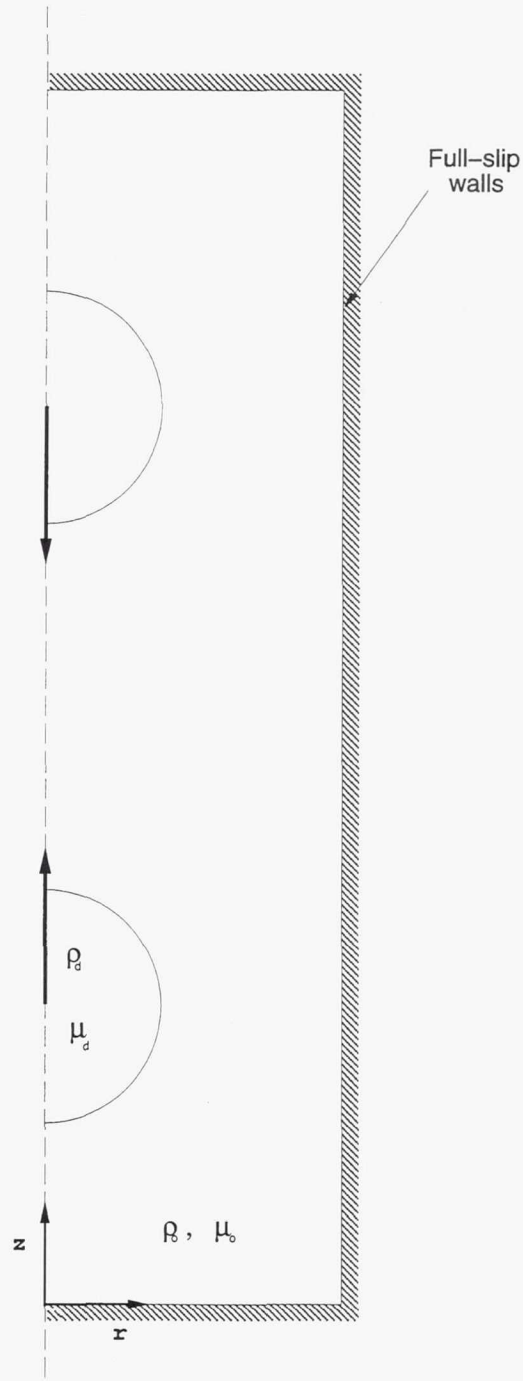

Figure 1: The computational setup. The axisymmetric domain is bounded by full-slip walls and resolved by a regular grid.

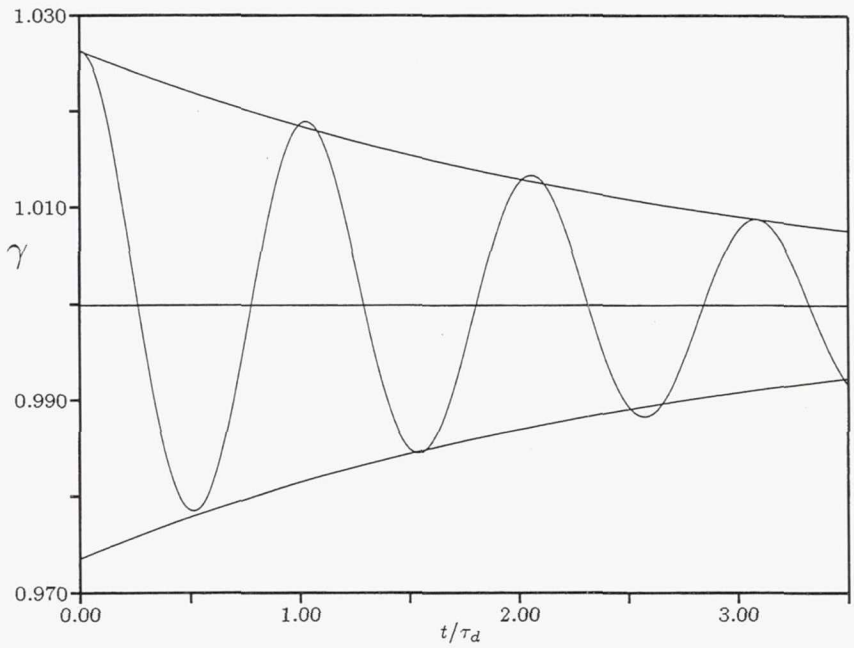

Figure 2: Comparison with analytical predictions. Oscillations of a single drop. The computed oscillation frequency is 3.77. Linearized theory gives $\omega_{th} = 3.88$ for completely inviscid drops. The rate of decay is also compared with the approximate theory of Lamb.

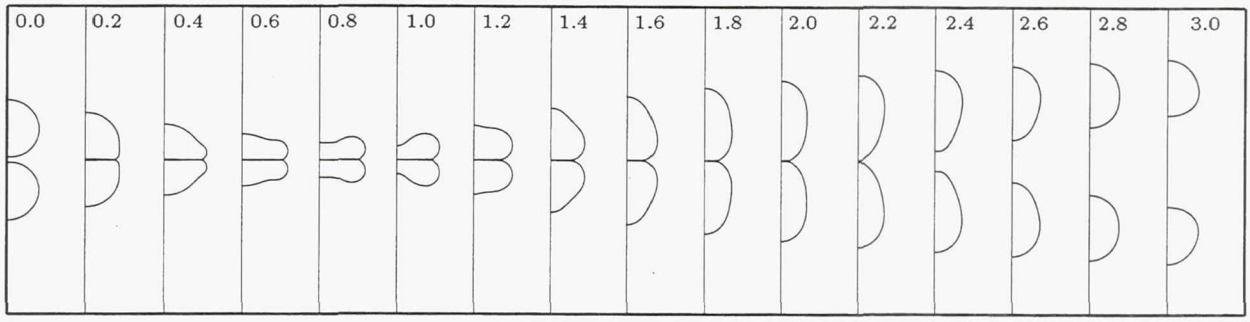

Figure 3: Collision of two drops. $We = 32$, $Re = 98$, $\rho_d/\rho_o = 15$, $\mu_d/\mu_o = 350$. The nondimensional time (scaled by the initial velocity and the drop diameter) is noted in each frame. The grid used here is 64×256 meshes.

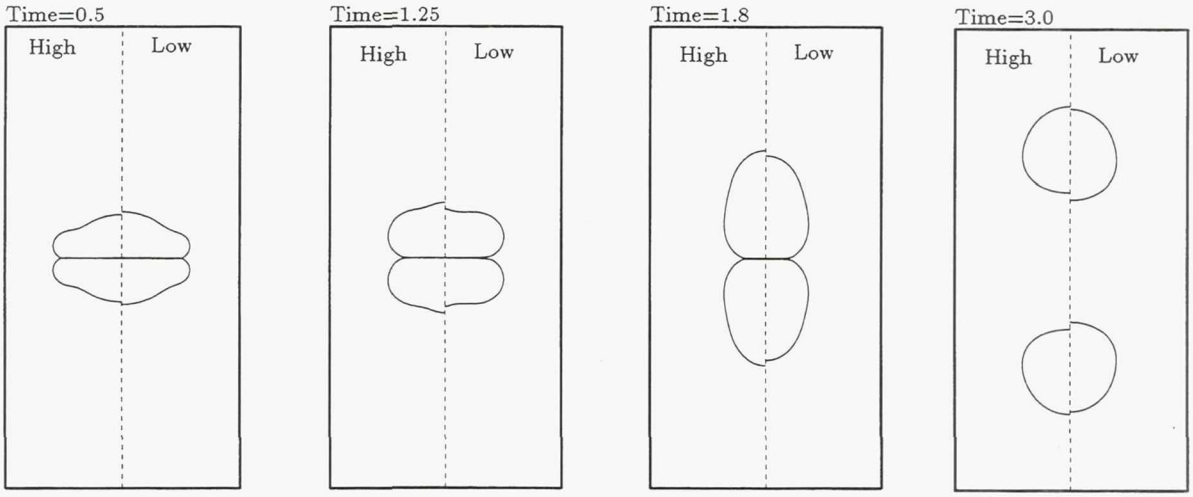

Figure 4: Resolution test. Selected frames from the computation in Figure 3 (left half) are compared with results obtained on twice as coarse grid (right half). The evolution on the coarser grid is slightly slower than on the finer grid.

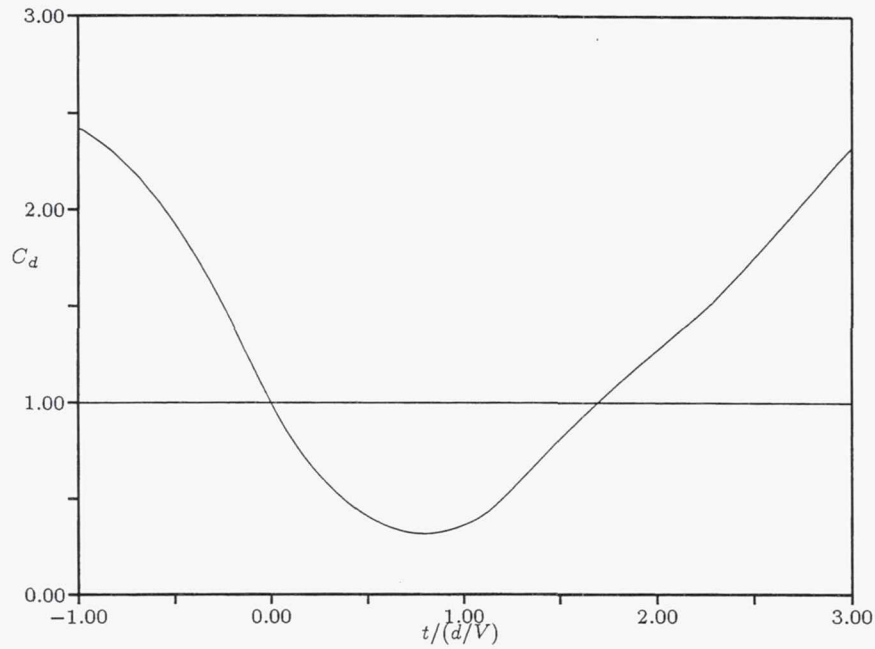

Figure 5a: Diagnostics for the simulations in Figures 3 and 4. The position of the center of mass of the drops versus time. The horizontal line marks the distance when the centers are one diameters apart.

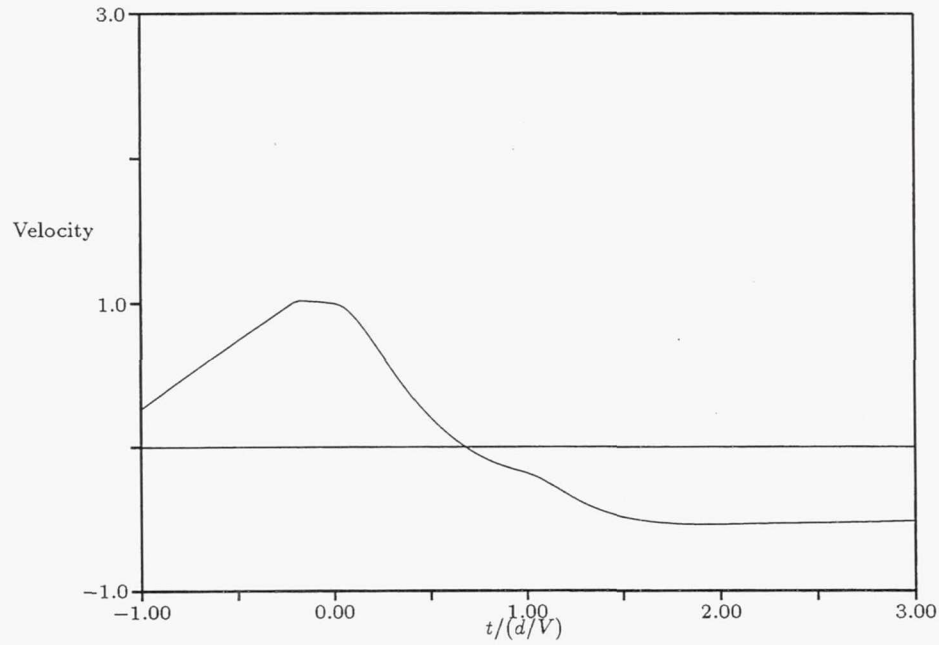

Figure 5b: The velocity of the center of mass of the drops versus time.

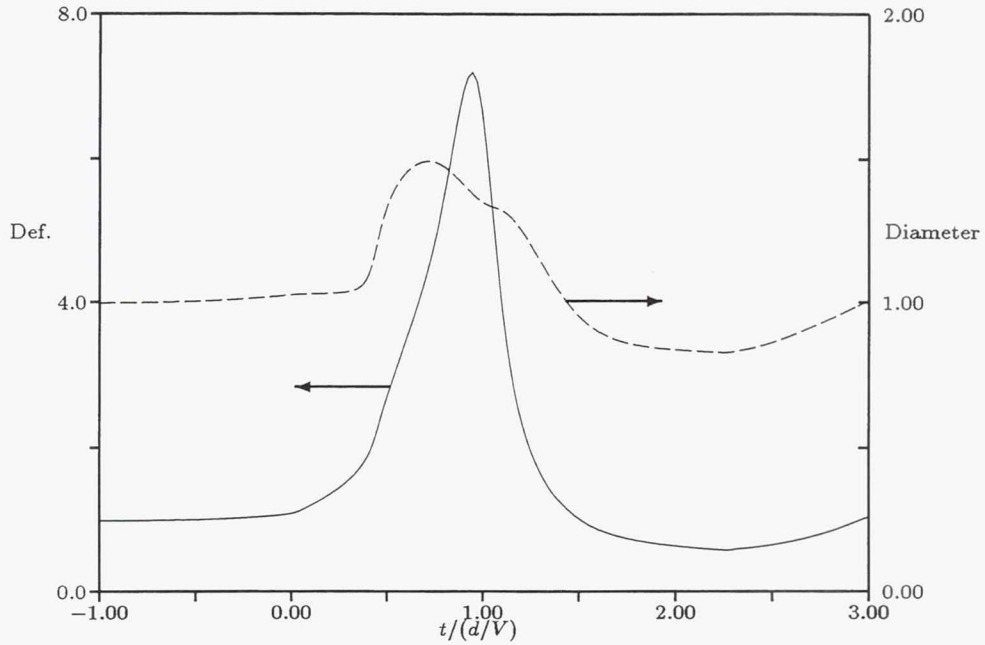

Figure 5c: "Deformation" of the drop versus time (solid line) and maximum diameter (dashed line).

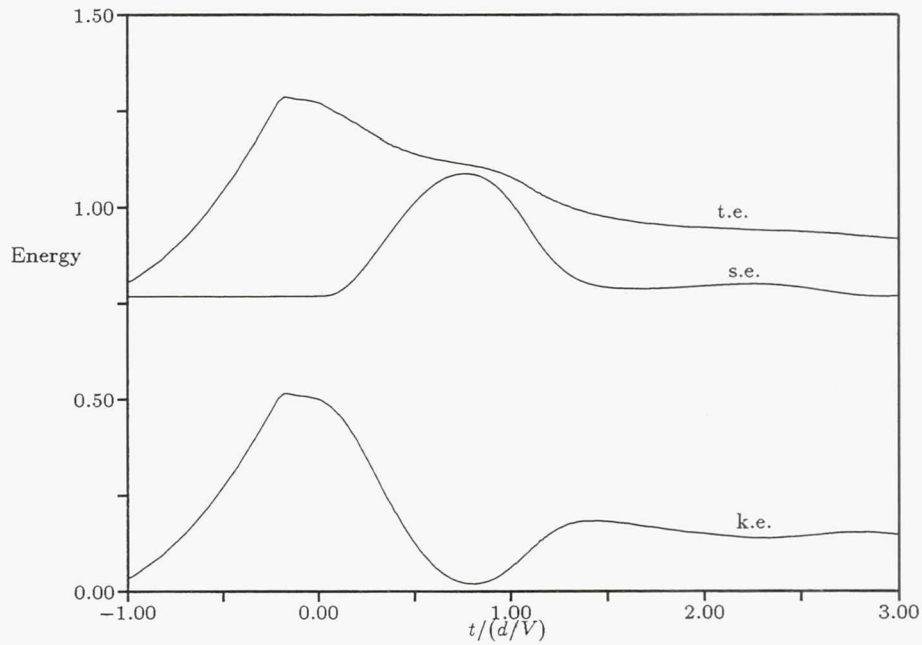

Figure 5d: Kinetic energy, surface tension energy and total energy versus time

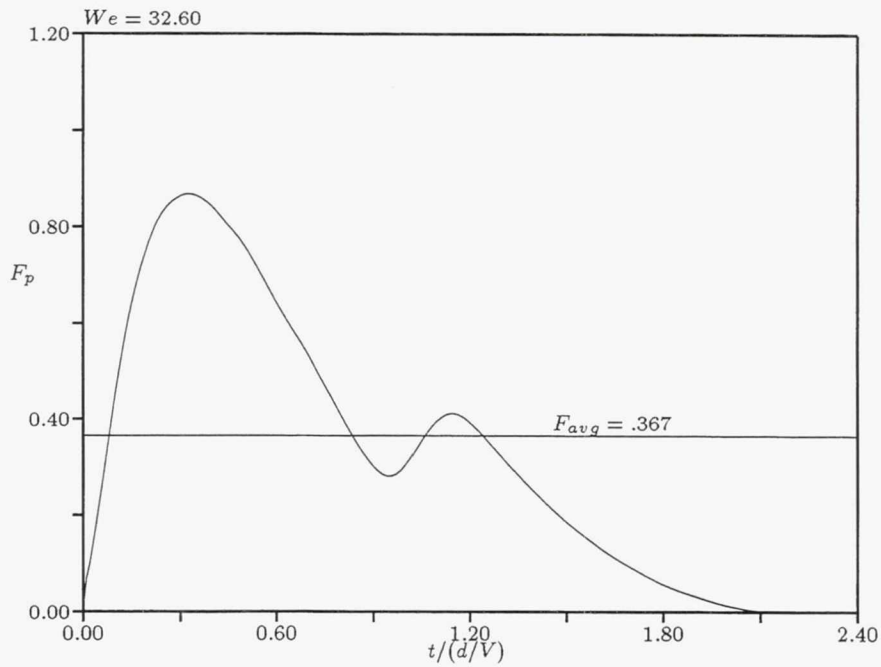

Figure 5e: The pressure force on the symmetry plane as a function of time. The horizontal line is the average force.

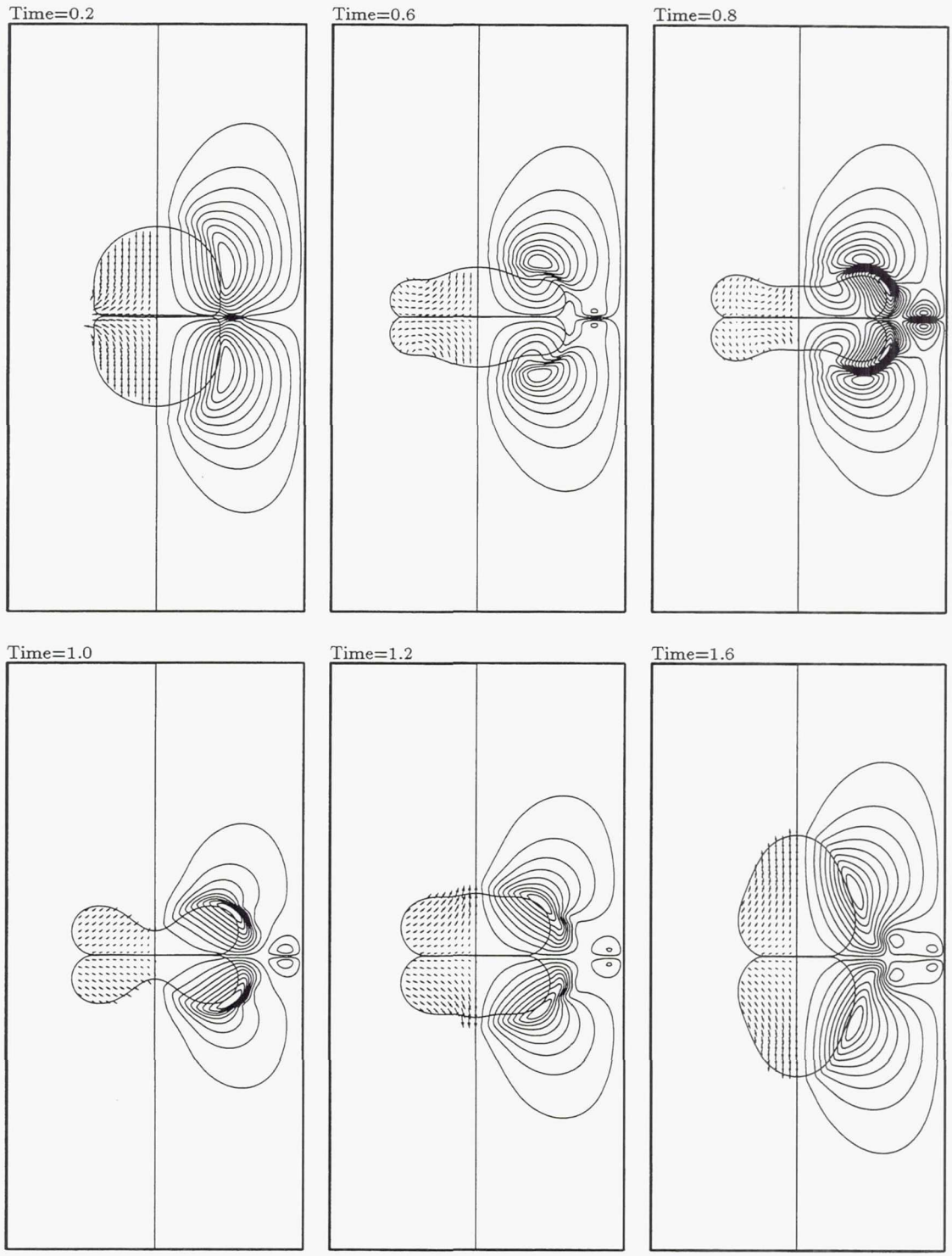

Figure 6: Velocity vectors inside the drops (left half) and streamlines (right half) for selected frames from the computations in figure 3.

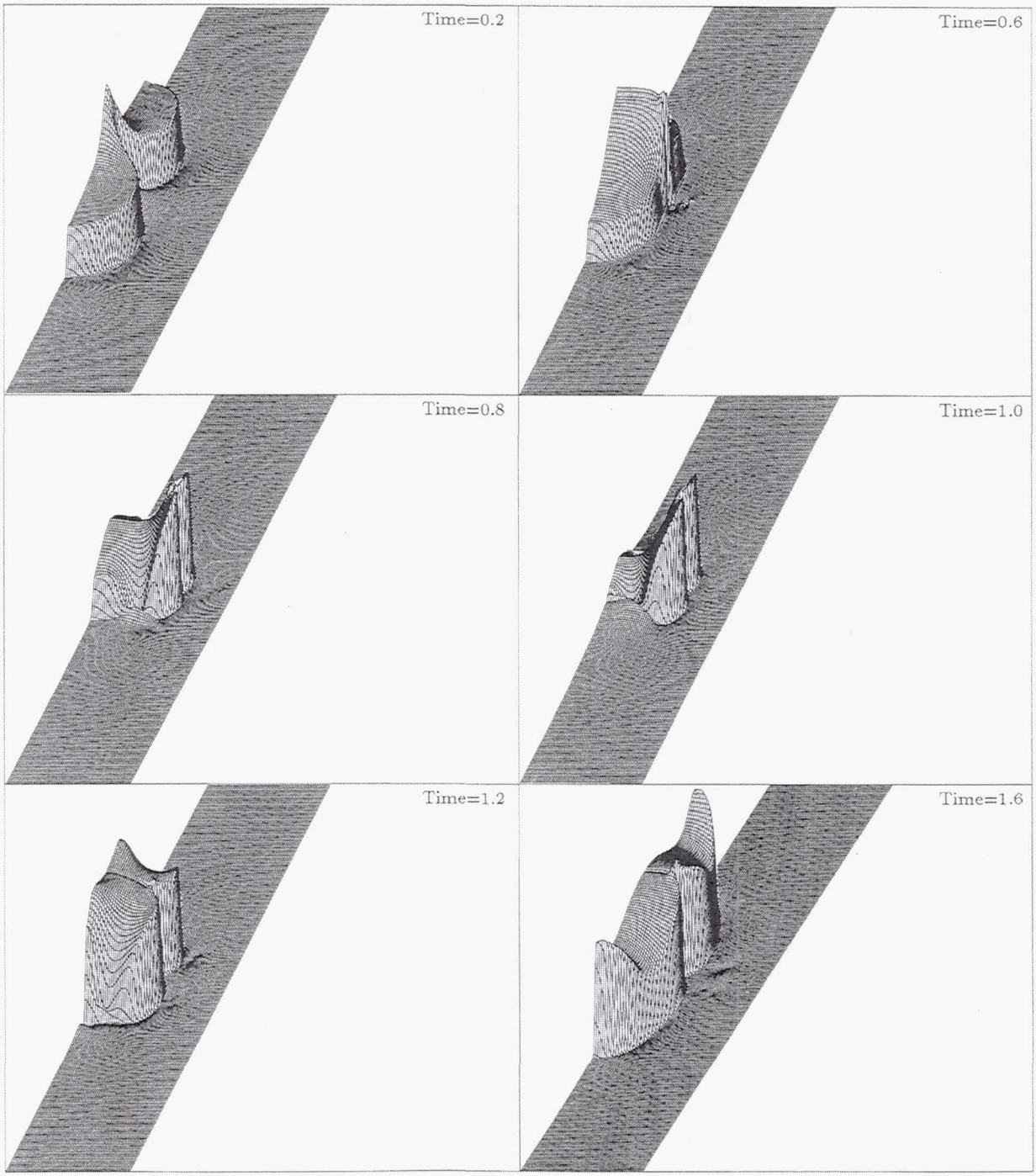

Figure 7: The pressure for selected frames from the computations in figure 3. Notice that the vertical scale is different in each frame. The times are the same as in figure 6.

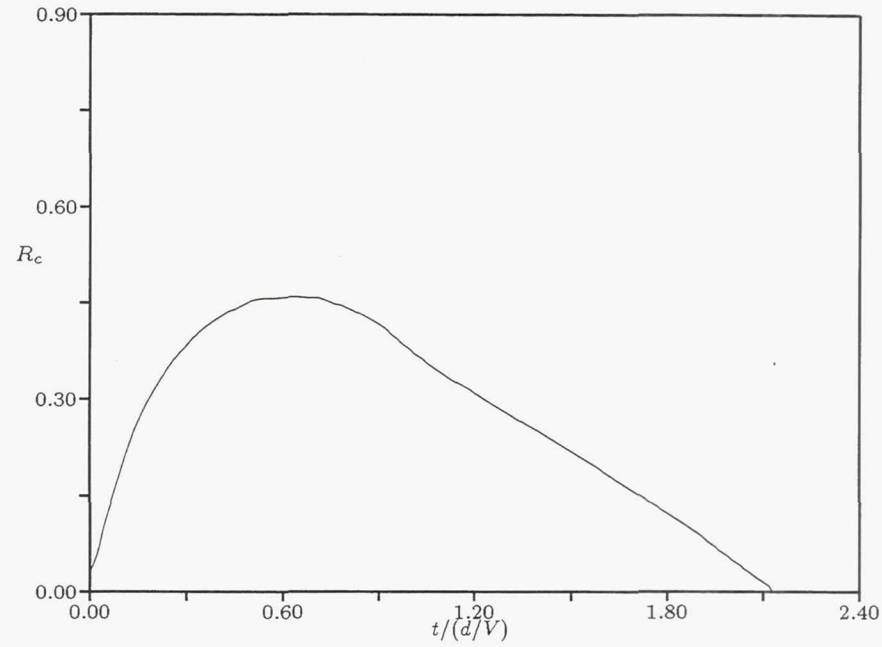

Figure 8a: The radial position of the outer edge of the contact plane between the drops as a function of time.

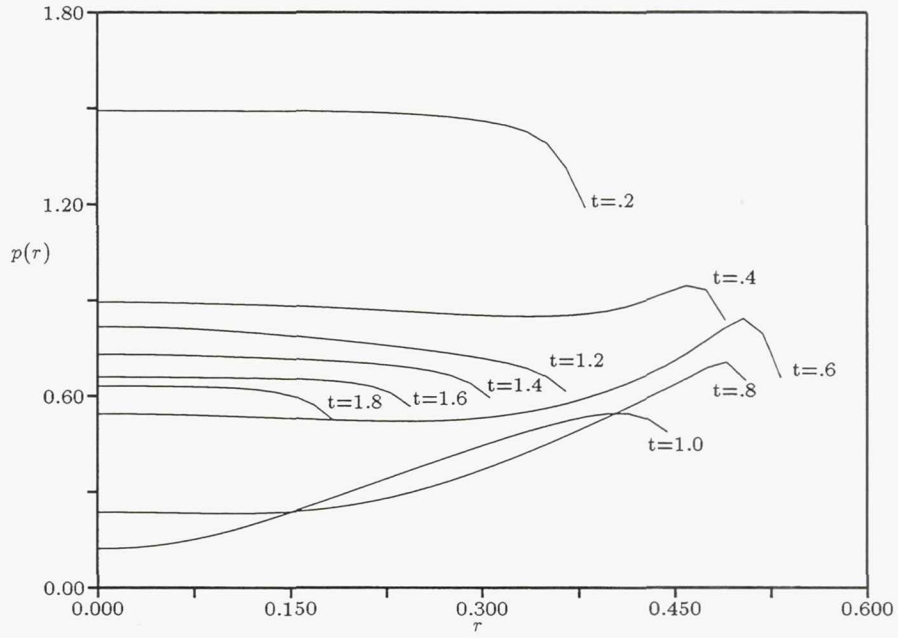

Figure 8b: Pressure on the symmetry plane between the drops as a function of radius for several times.

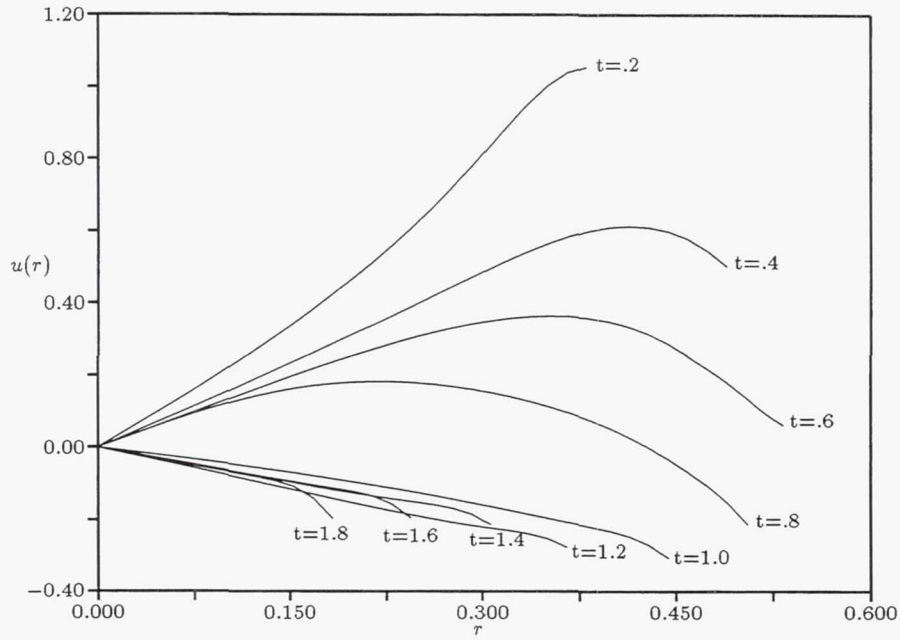

Figure 8c: Radial velocity on the symmetry plane between the drops as a function of radius for several times.

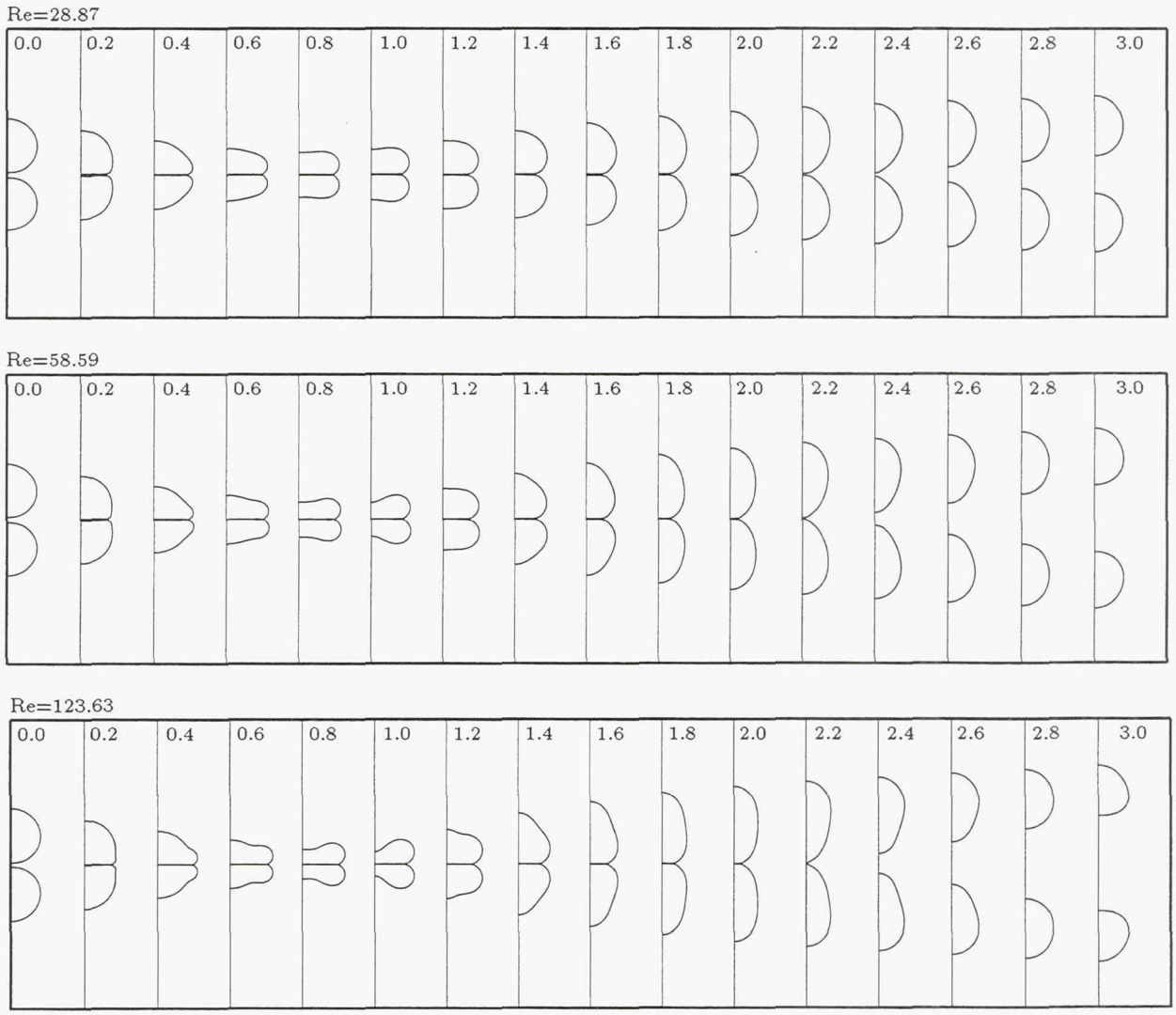

Figure 9: Selected frames for the collision of two drops at $We = 30$, $\rho_d/\rho_o = 15$, $\mu_d/\mu_o = 350$, and different Reynolds numbers. The nondimensional time (based on initial velocity and drop diameter) is noted on each frame. (a) $Re = 28$. (b) $Re = 58$. (c) $Re = 120$.

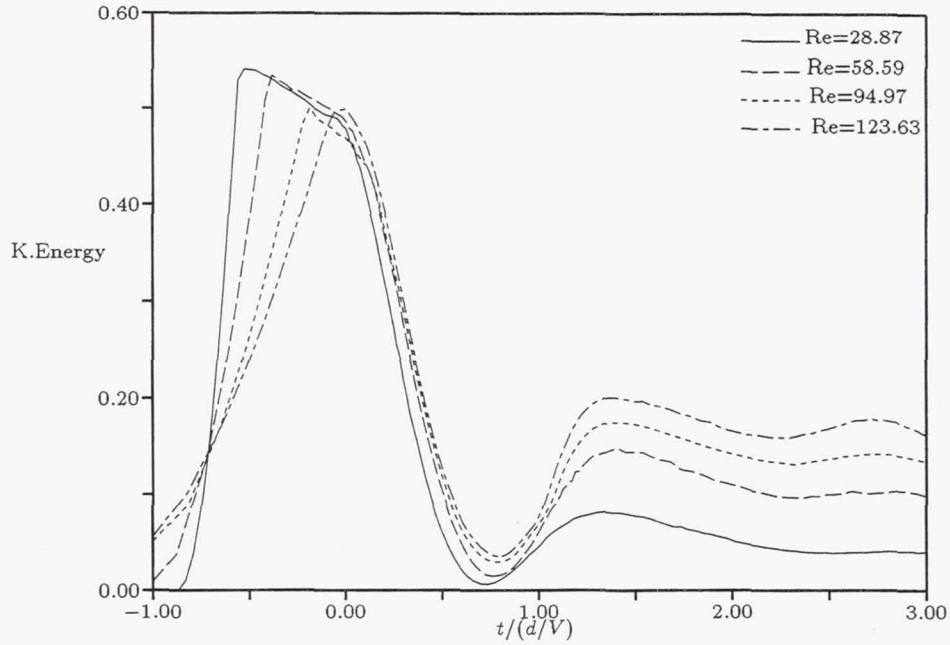

Figure 10a: Kinetic energy for the runs in figure 9 and 3 versus time.

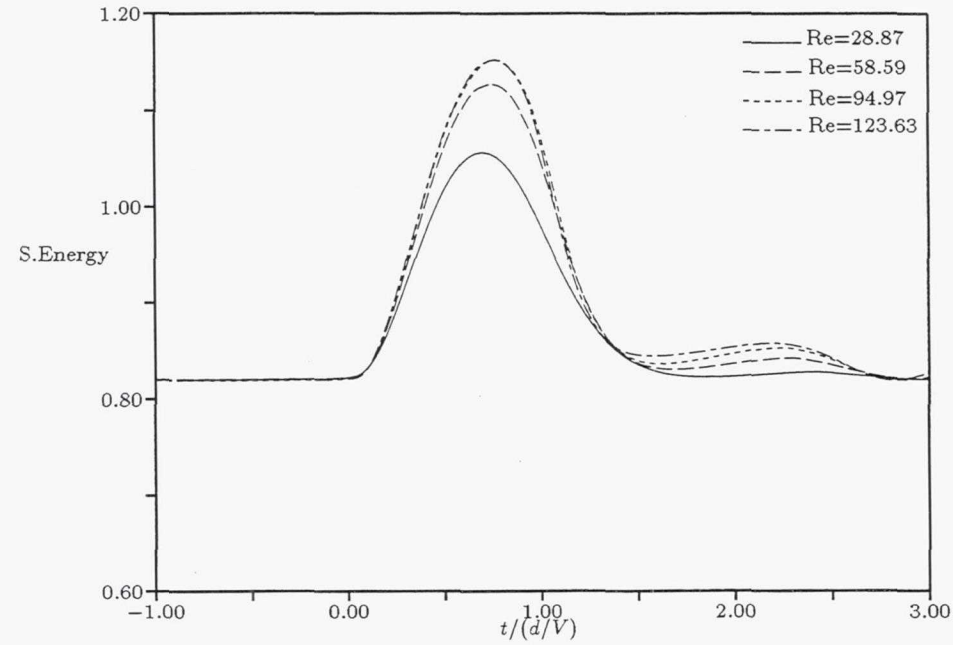

Figure 10b: Surface energy for the runs in figure 9 and 3 versus time.

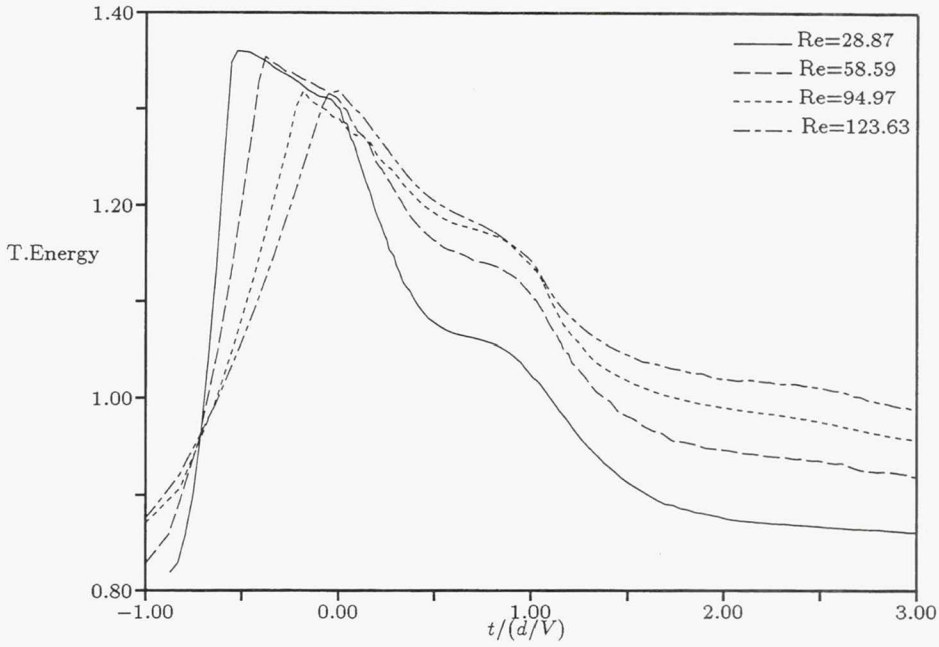

Figure 10c: Total energy for the runs in figure 9 and 3 versus time.

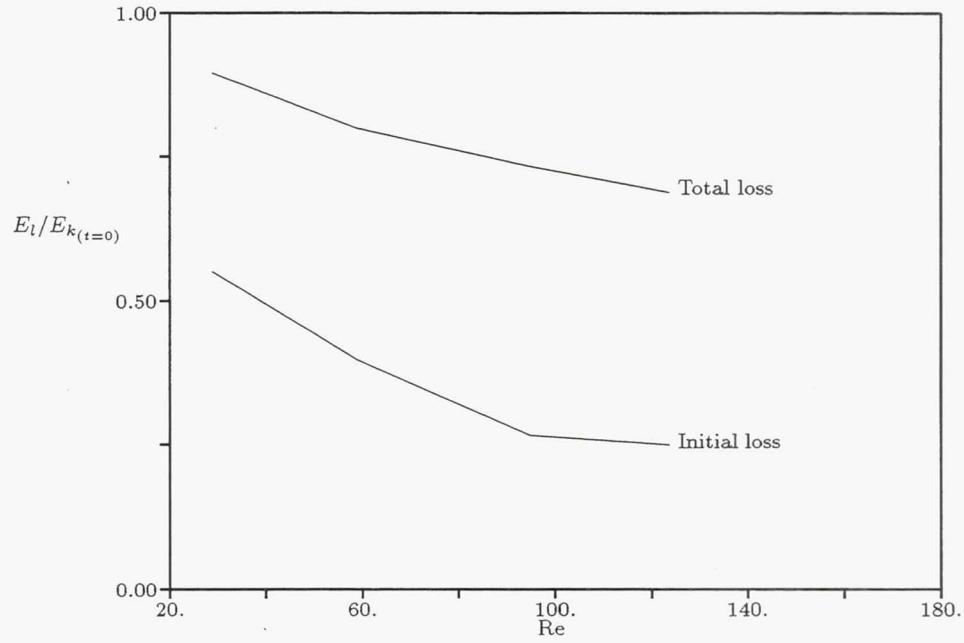

Figure 11a: Diagnostics for the simulations in Figure 9 and 3. Loss of energy versus Reynolds number. The lower line shows the loss in total energy during first half of the collision (up to maximum deformation) and the top line shows the total loss during the collision.

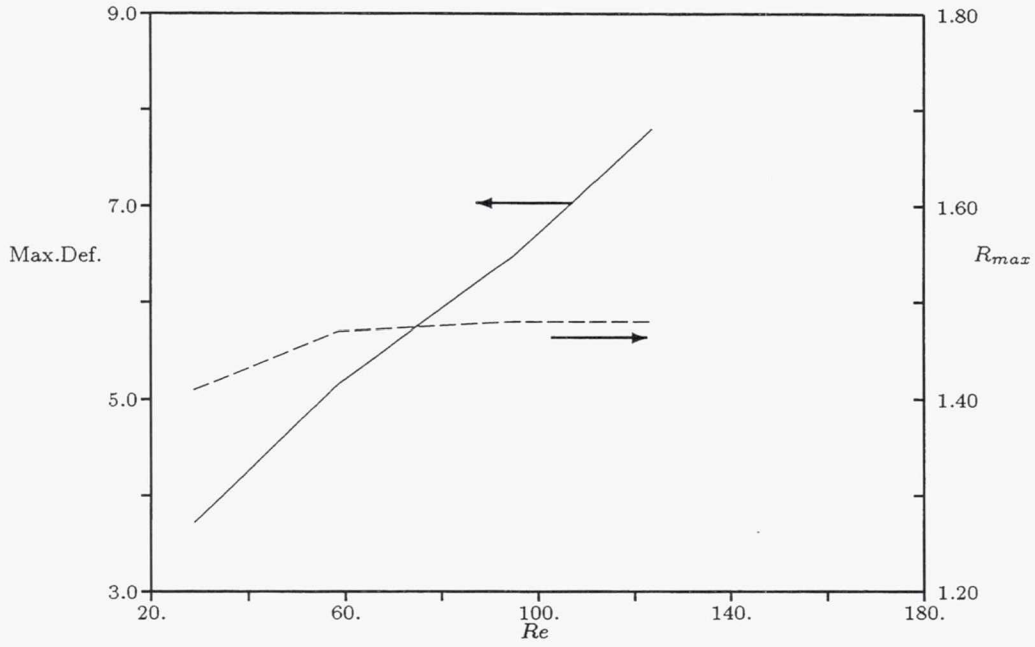

Figure 11b: Maximum deformation (solid line) and maximum radius (dashed line) versus Reynolds number.

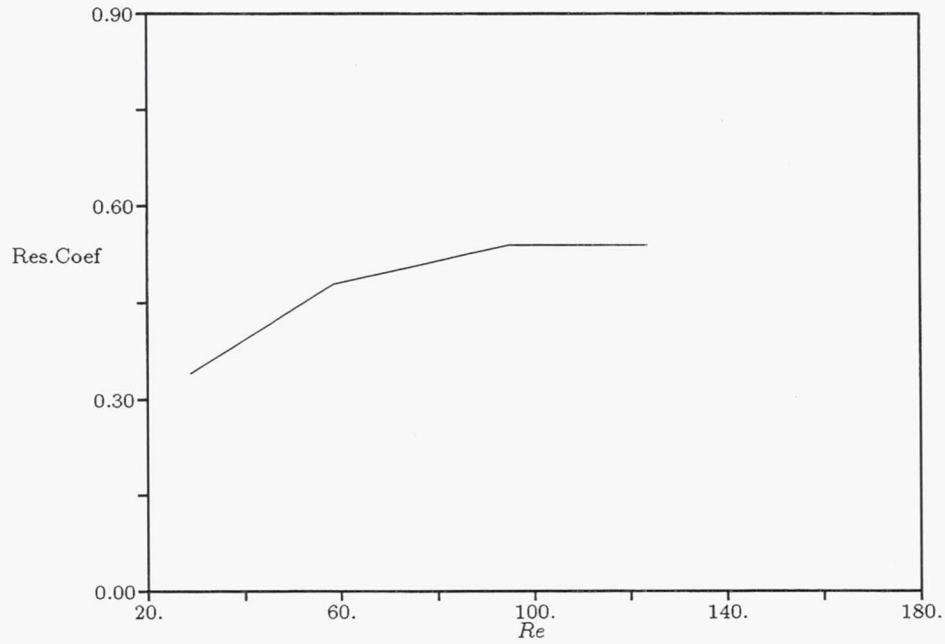

Figure 11c: Coefficient of restitution versus Reynolds number.

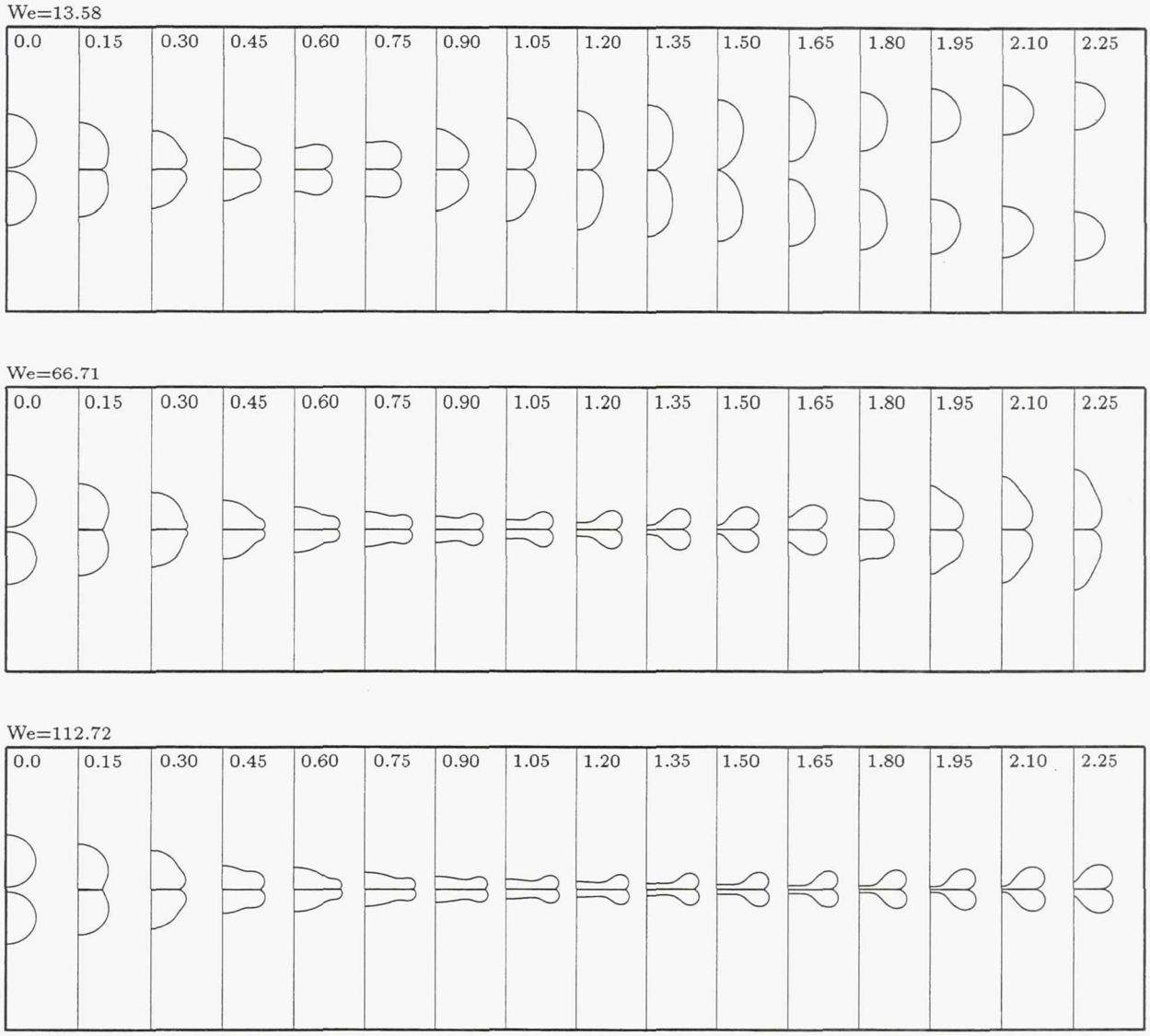

Figure 12: Selected frames for the collision of two drops at $Re = 96$, $\rho_d/\rho_o = 15$, $\mu_d/\mu_o = 350$, and different We. The nondimensional time (based on initial velocity and drop diameter) is noted on each frame. (a) $We = 13$. (b) $We = 66.9$. (c) $We = 112$.

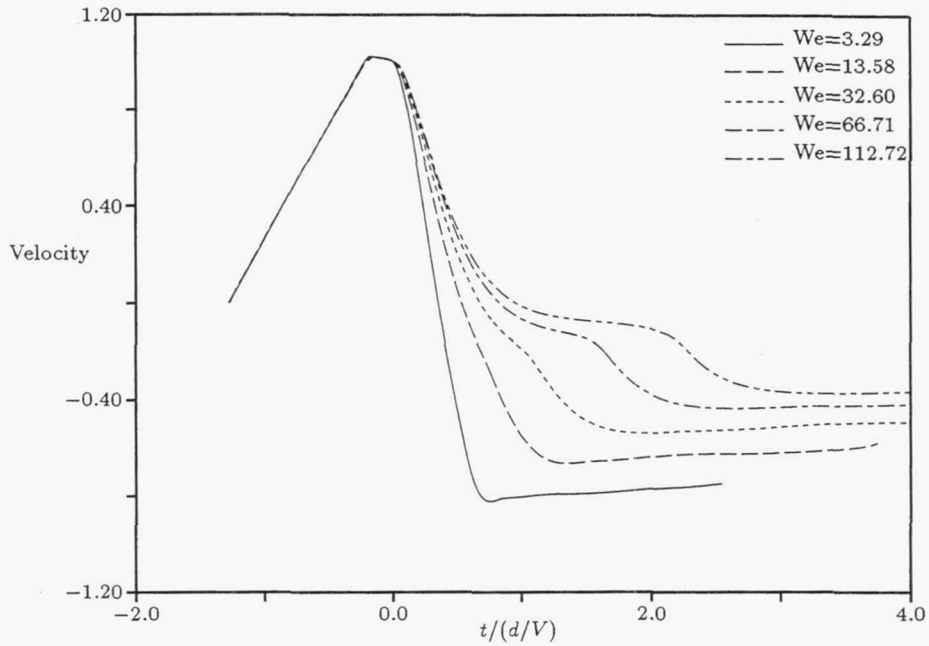

Figure 13a: Velocities versus time for the runs in Figures 12 and 3 versus nondimensional time. Time is nondimensionalized by the initial velocity of the drop and its diameter.

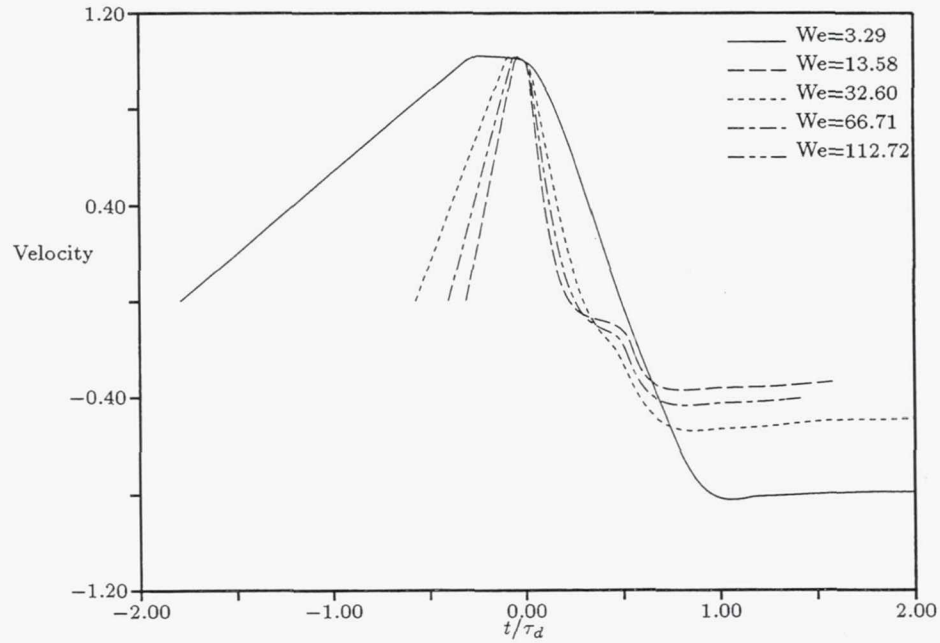

Figure 13b: Time is nondimensionalized by the the fundamental period of the oscillations of a single drop.

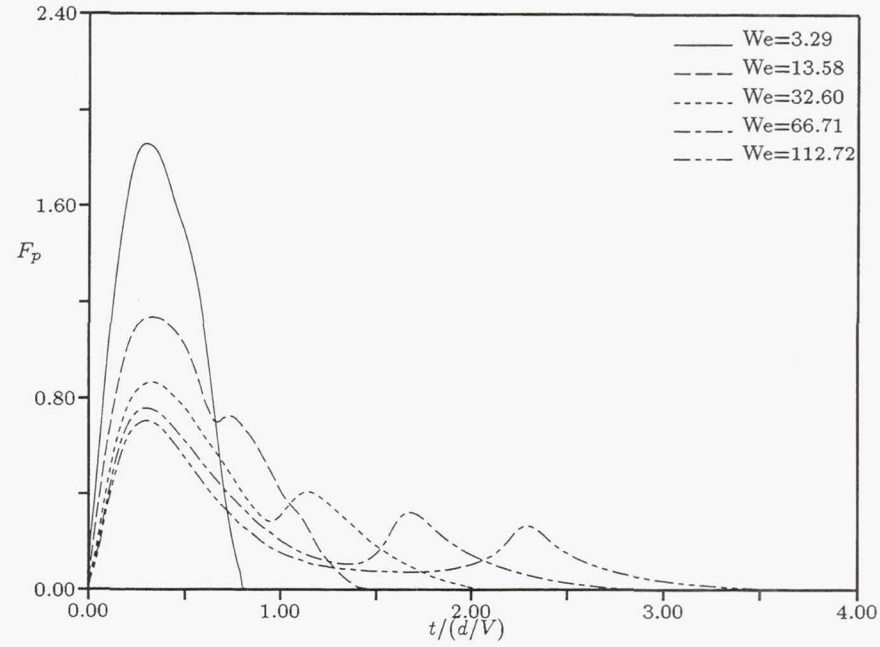

Figure 14: Force on the symmetry plane versus time (scaled by the initial velocity of the drop and its diameter).

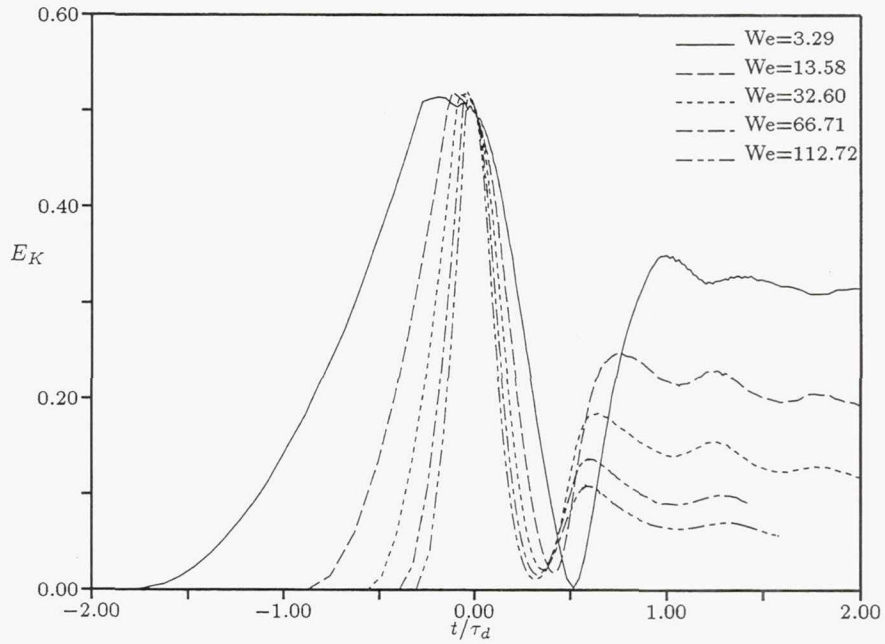

Figure 15a: Kinetic energy for the runs in Figures 12 and 3 versus time.

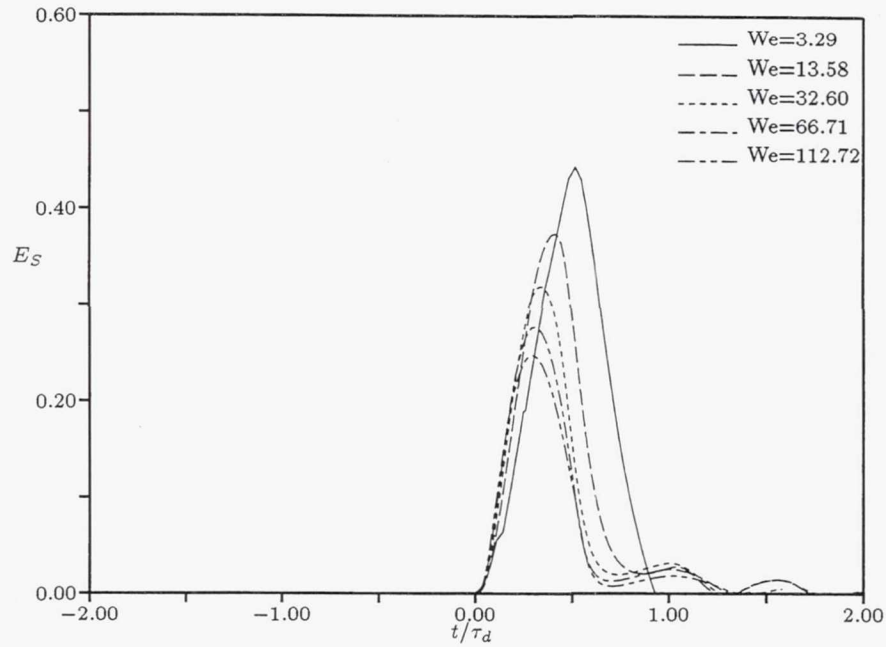

Figure 15b: Surface energy for the runs in Figures 12 and 3 versus time.

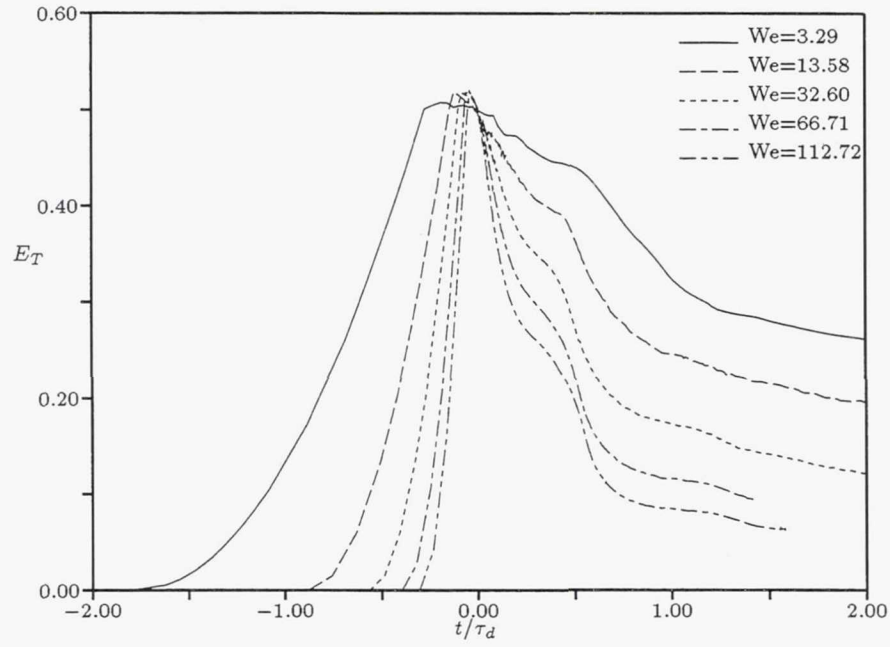

Figure 15c: Total energy for the runs in Figures 12 and 3 versus time.

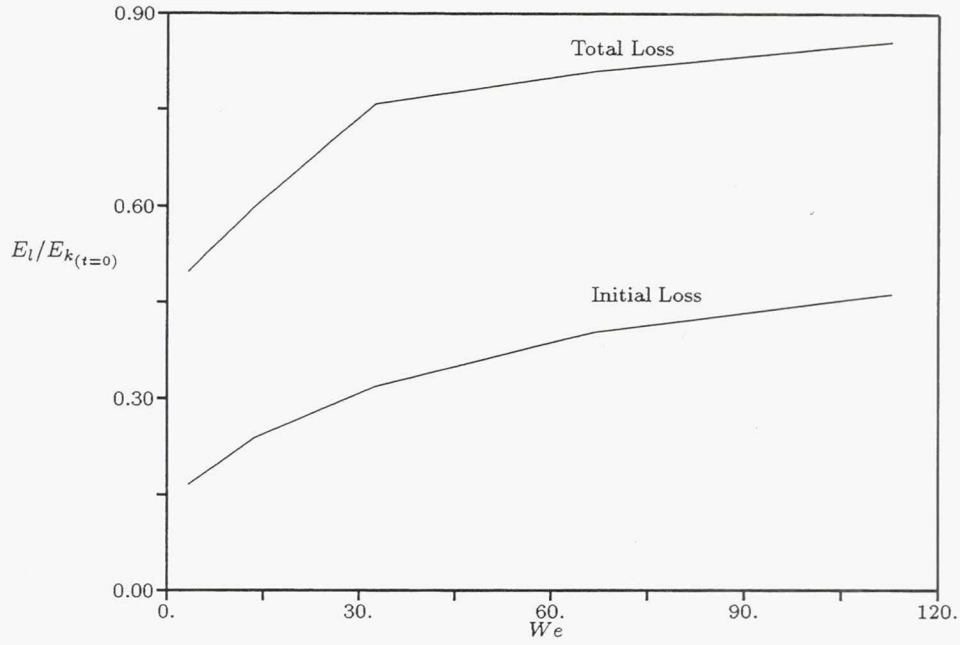

Figure 16a: Diagnostics for the simulations in Figures 12 and 3. Loss of energy versus Weber number. The lower line shows the loss in total energy during first half of the collision (up to maximum deformation) and the top line shows the total loss during the collision.

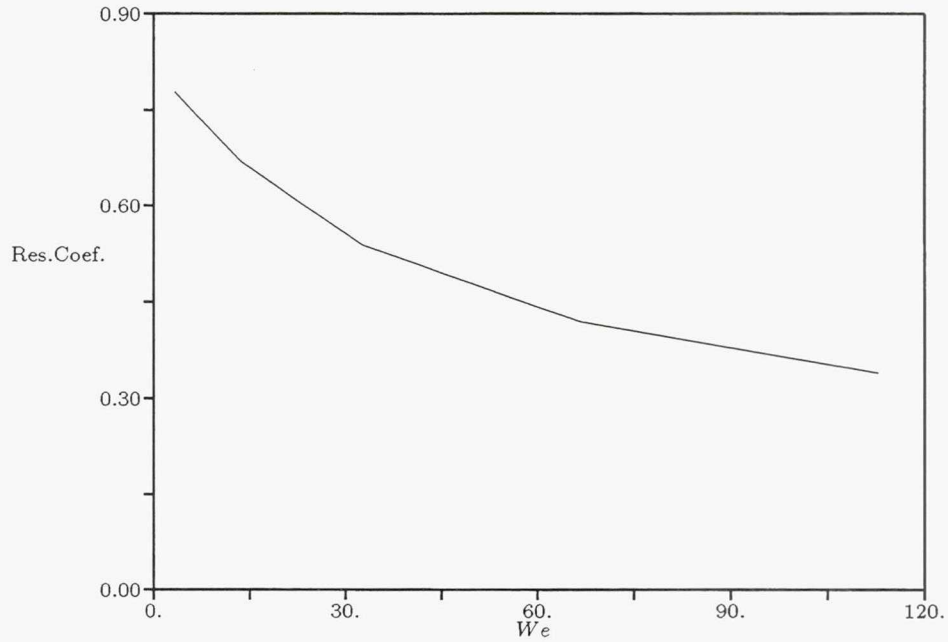

Figure 16b: Coefficient of restitution versus Weber number.

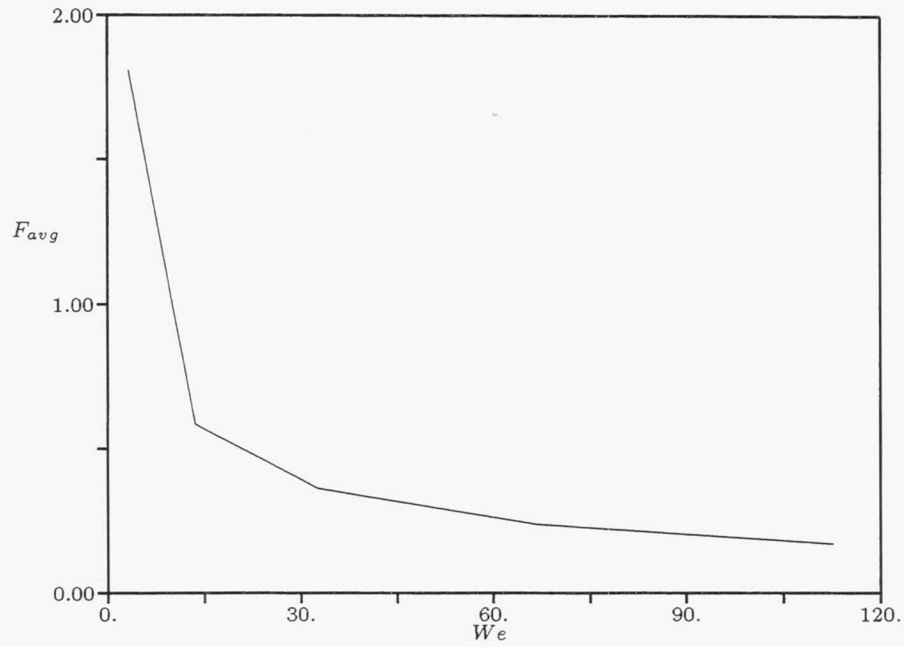

Figure 16c: Average collision force versus Weber number.

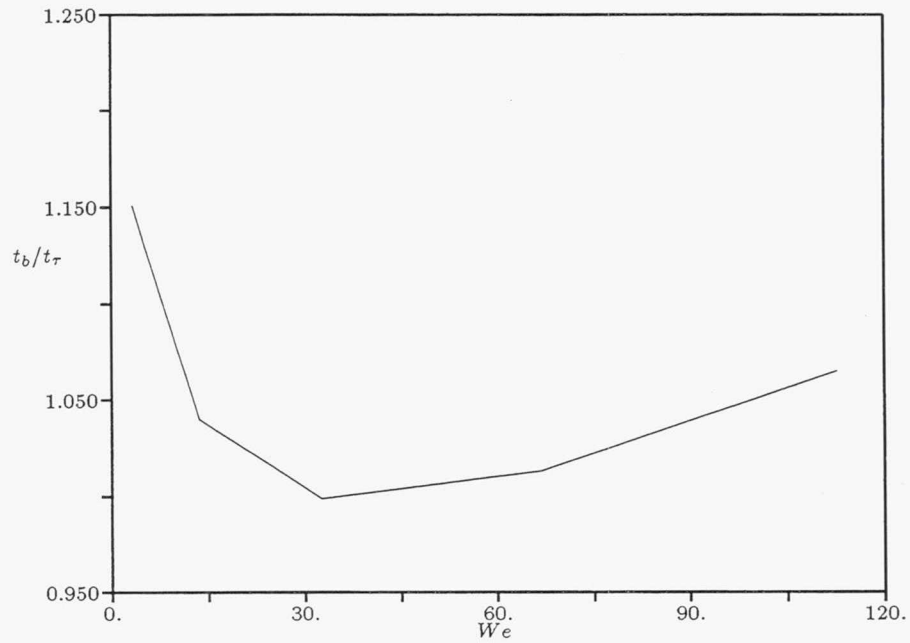

Figure 16d: Time of collision in units of period of oscillation of a single drop versus Weber number.

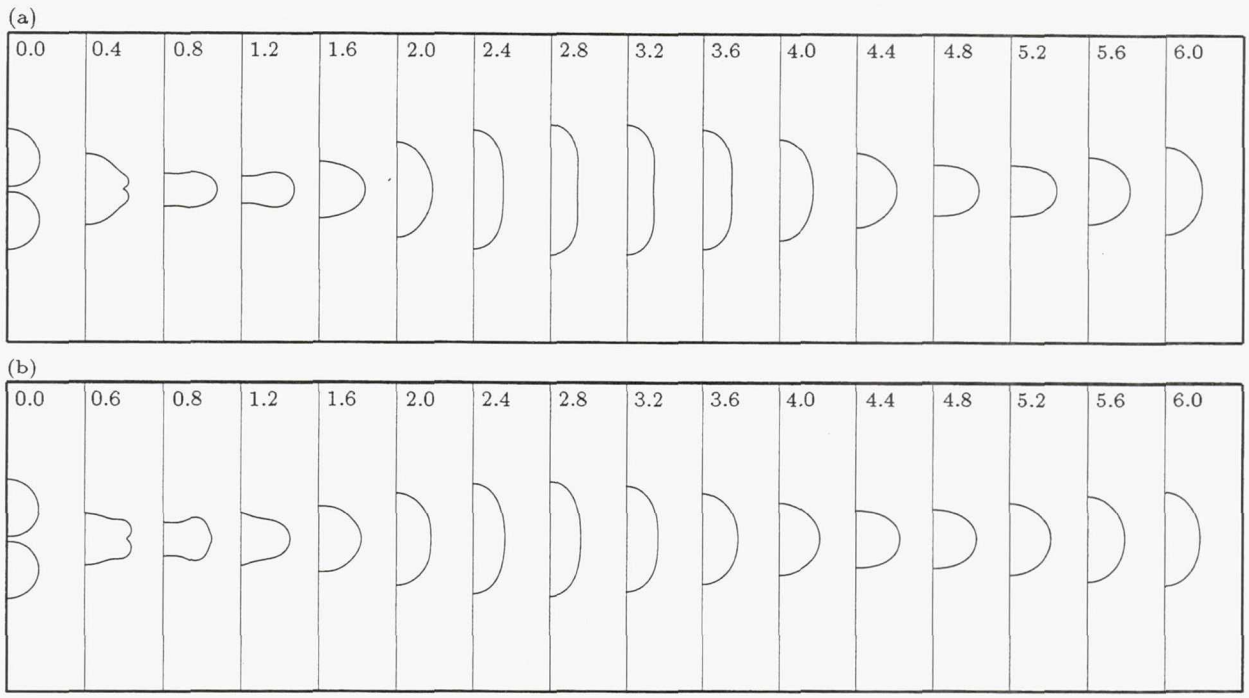

Figure 17: The evolution following rupture of the interface separating the drops for the simulation in Figure 3. In both cases the drops coalesce permanently. (a) Rupture at $t = 0.4$. (b) Rupture at $t = 0.6$.

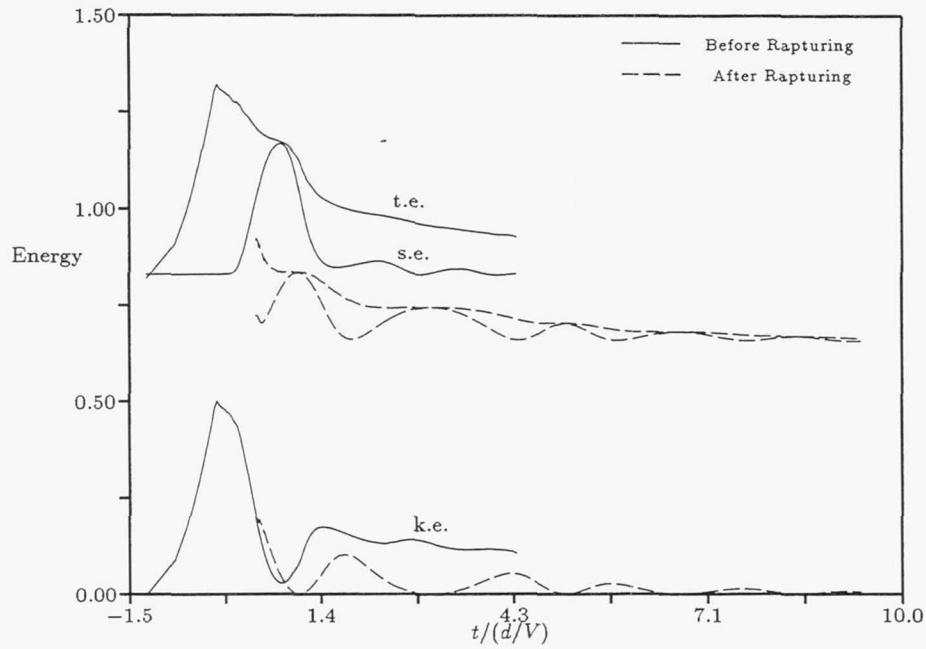

Figure 18a: The energy versus time for the simulations in figure 17a.

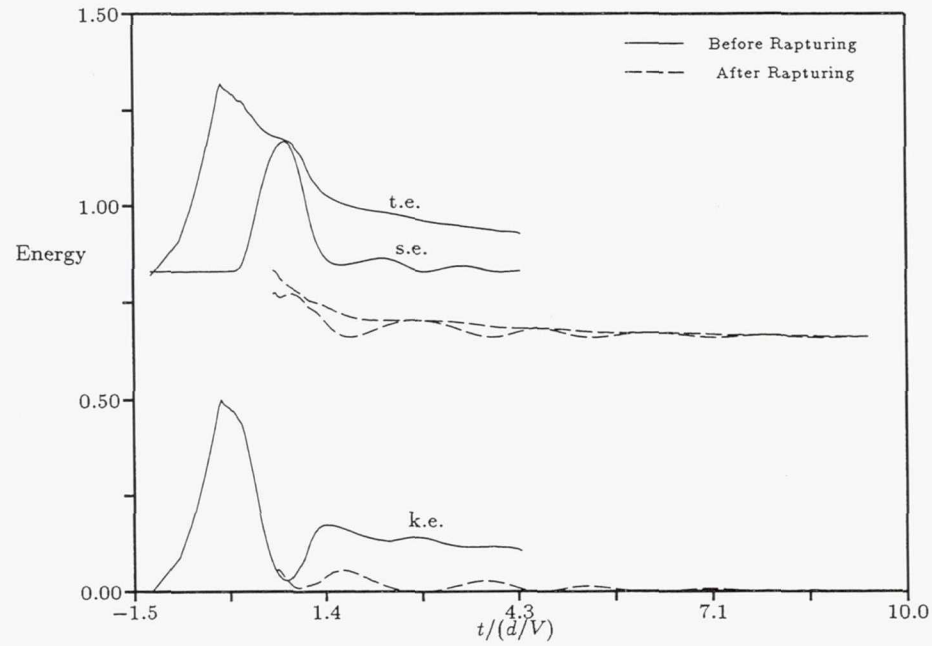

Figure 18b: The energy versus time for the simulations in figure 17b.

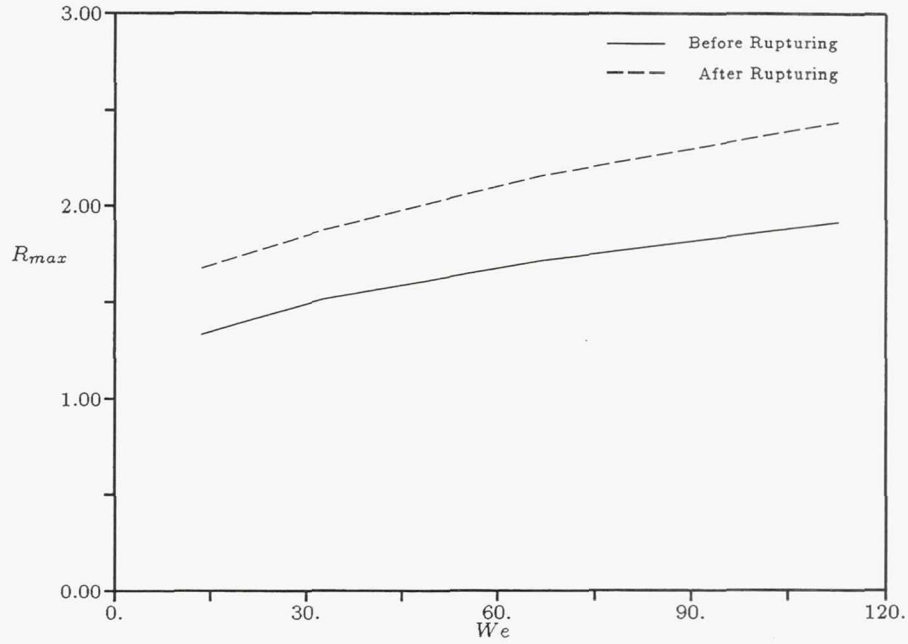

Figure 19a: The evolution following rupture of the interface separating the drops at $t = 0.2$ for $Re = 98$, $\rho_d/\rho_o = 15$, and $\mu_d/\mu_o = 350$ (same conditions as in figure 12). The maximum radius versus Weber number.

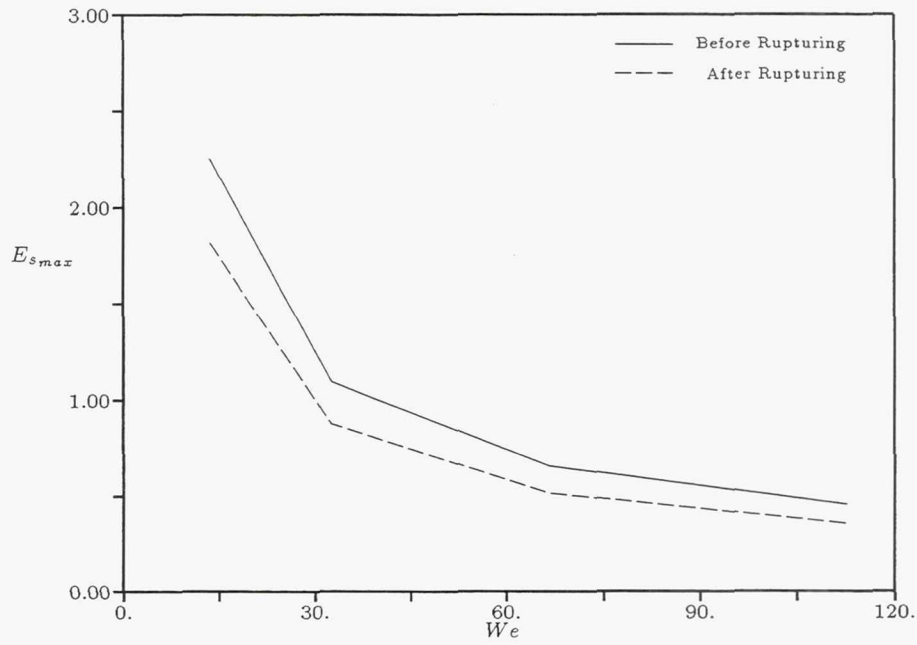

Figure 19b: The maximum surface tension energy versus Weber number.

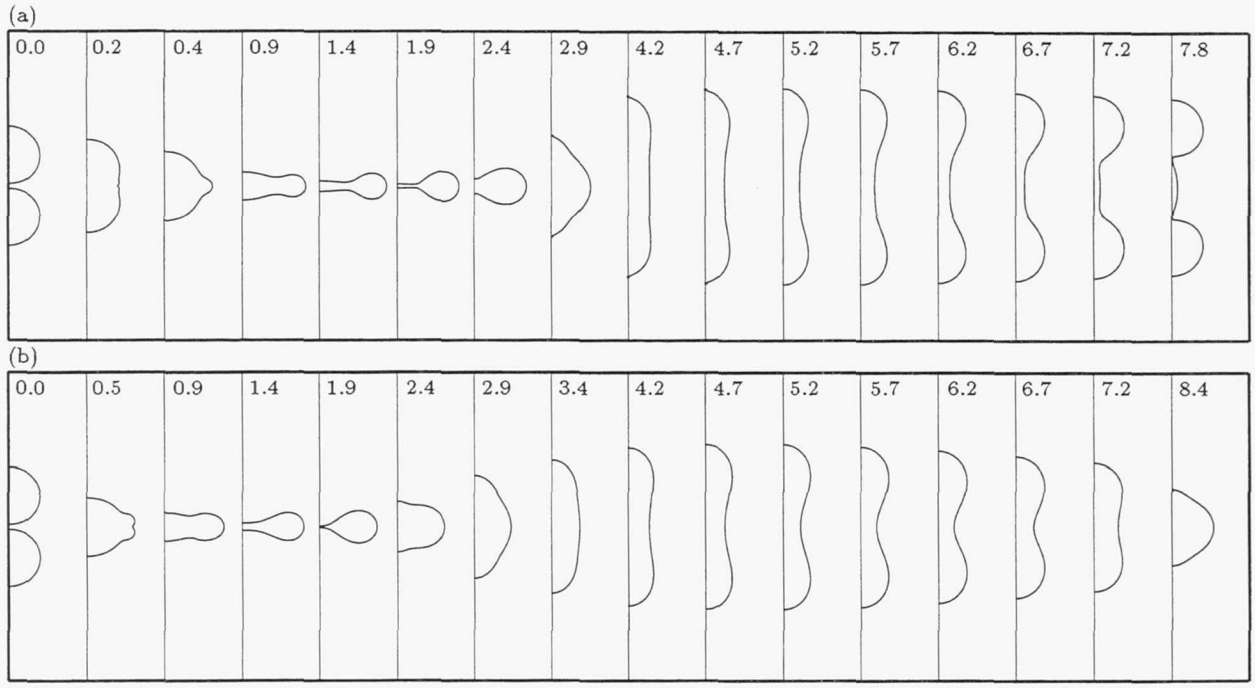

Figure 20: The evolution following rupture of the interface separating the drops for $We = 65$, $Re = 140$, $\rho_d/\rho_o = 15$, and $\mu_d/\mu_o = 350$. In (a) the drops eventually separate again, following initial coalescence, but in (b) the drops remain one. (a) Rupture at $t = 0.2$. (b) Rupture at $t = 0.5$.

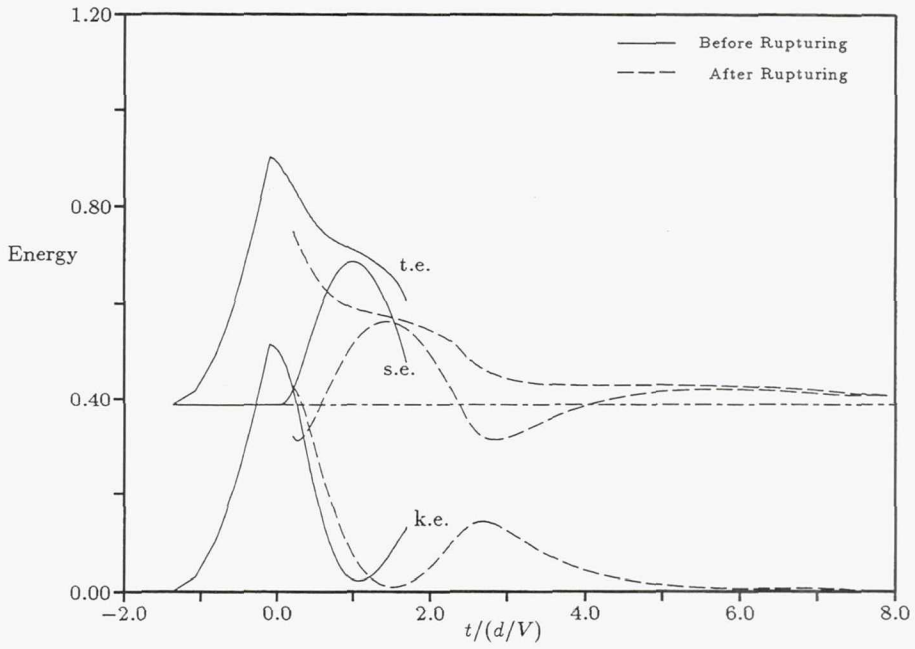

Figure 21a: The energy versus time for the simulations in figure 19a as in Figure 20.

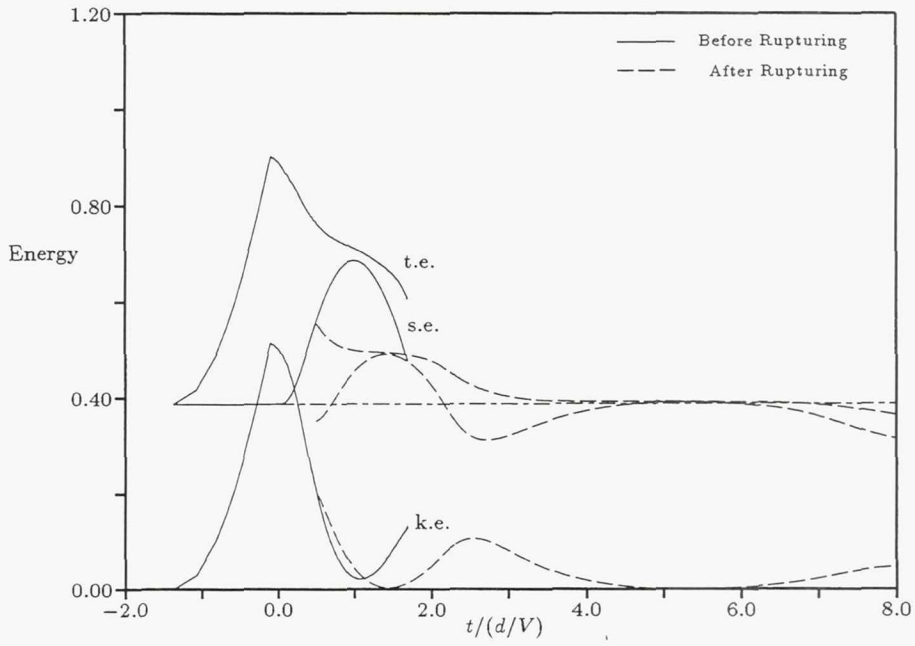

Figure 21b: The energy versus time for the simulations in figure 19b as in Figure 20.

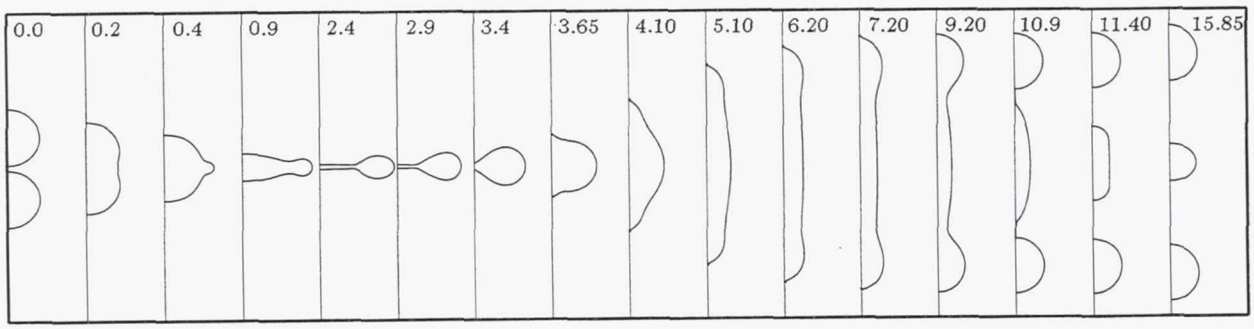

Figure 22: The evolution following rupture of the interface separating the drops for $We = 115$, $Re = 185$, $\rho_d/\rho_o = 15$, and $\mu_d/\mu_o = 350$.

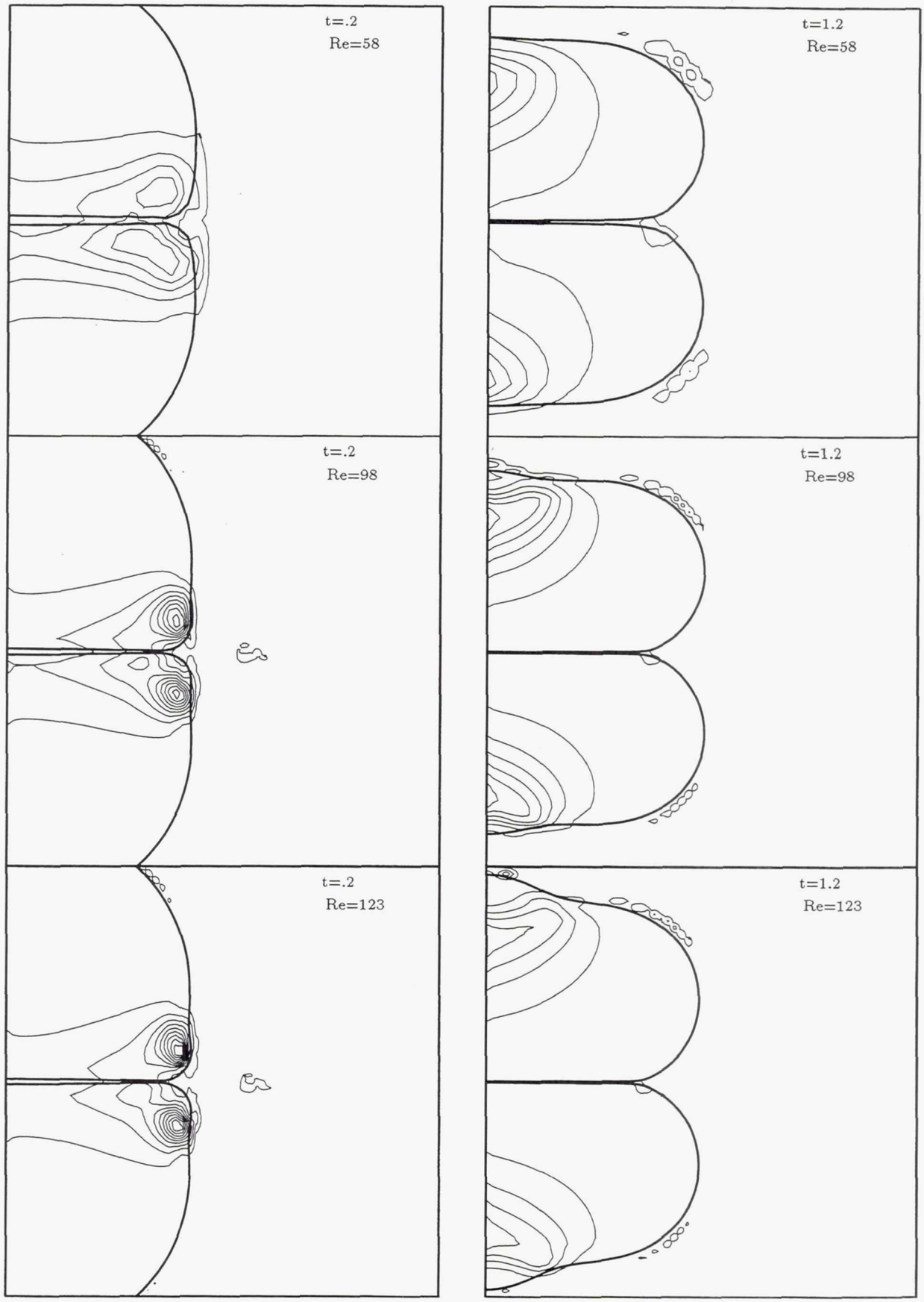

Figure 23: Dissipation per unit volume for bouncing drops. t=0.2 for the left column and t=1.2 for the right column. Re=58 for the top row; Re=98 for the middle row; and Re=123 for the bottom row.

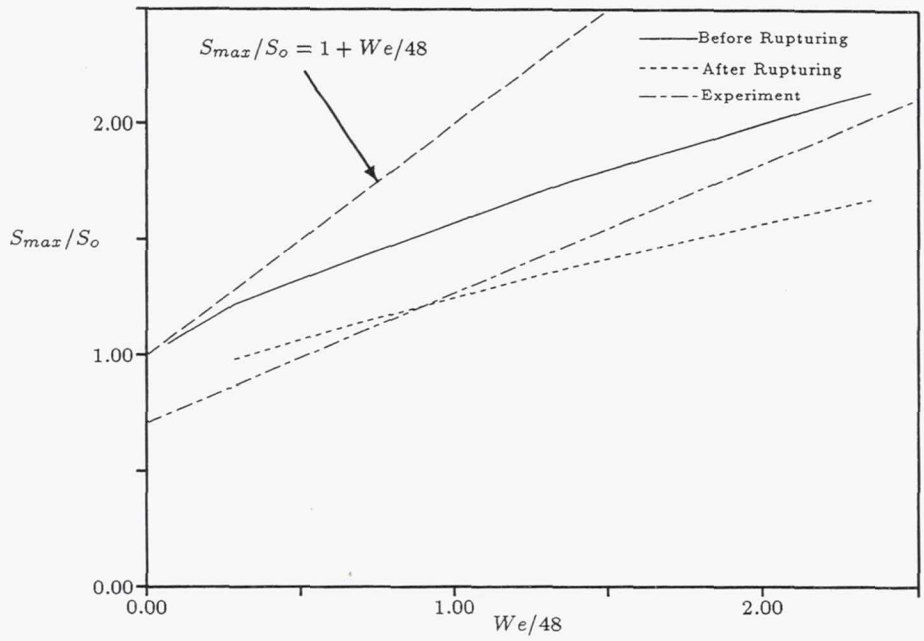

Figure 24: Maximum surface area. The top line is the theoretical prediction for no losses. The solid line is for bouncing drops and the dashed line is for drops that coalesce. The dash-dot line is a best fit to experimental data from Jiang *et al.*

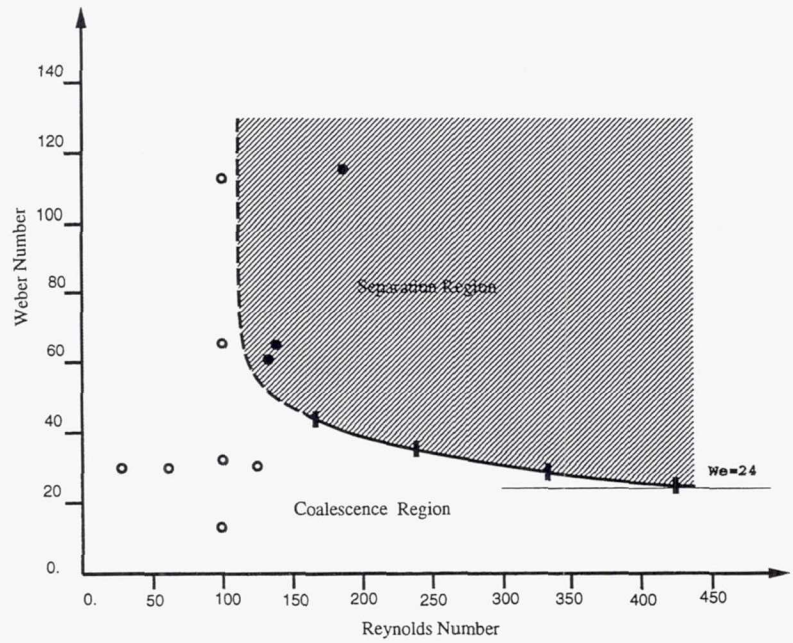

Figure 25: The boundaries between coalescing and separating collisions in the Re-We plane. Open circles are computations where the drops coalesced permanently, dark circles are computations where the drops separated again. The solid line is data from Jiang *et al* (1992) and the dashed line is an extrapolation based on the computational results.

REPORT DOCUMENTATION PAGE

Form Approved
OMB No. 0704-0188

1. AGENCY USE ONLY (*Leave blank*)	2. REPORT DATE	3. REPORT TYPE AND DATES COVERED
	November 1993	Technical Memorandum

4. TITLE AND SUBTITLE

Head-On Collision of Drops – A Numerical Investigation

5. FUNDING NUMBERS

WU–505–90–5K

6. AUTHOR(S)

M.R. Nobari, Y.-J. Jan, and G. Tryggvason

7. PERFORMING ORGANIZATION NAME(S) AND ADDRESS(ES)

National Aeronautics and Space Administration
Lewis Research Center
Cleveland, Ohio 44135–3191

8. PERFORMING ORGANIZATION REPORT NUMBER

E–8219

9. SPONSORING/MONITORING AGENCY NAME(S) AND ADDRESS(ES)

National Aeronautics and Space Administration
Washington, D.C. 20546–0001

10. SPONSORING/MONITORING AGENCY REPORT NUMBER

NASA TM–106394
ICOMP–93–45

11. SUPPLEMENTARY NOTES

M.R. Nobari and Y.-J. Jan, The University of Michigan, Department of Mechanical Engineering, Ann Arbor, Michigan 48109; and G. Tryggvason, Institute for Computational Mechanics in Propulsion, NASA Lewis Research Center, and The University of Michigan, Department of Mechanical Engineering, Ann Arbor, Michigan 48109, (work funded under NASA Cooperative Agreement NCC3–233). ICOMP Program Director, Louis A. Povinelli, (216) 433–5818.

12a. DISTRIBUTION/AVAILABILITY STATEMENT

Unclassified - Unlimited
Subject Category 34

12b. DISTRIBUTION CODE

13. ABSTRACT (*Maximum 200 words*)

The head-on collision of equal sized drops is studied by full numerical simulations. The Navier-Stokes equations are solved for the fluid motion both inside and outside the drops using a front tracking/finite difference technique. The drops are accelerated toward each other by a body force that is turned off before the drops collide. When the drops collide, the fluid between them is pushed outward leaving a thin layer bounded by the drop surface. This layer gets progressively thinner as the drops continue to deform and in several of our calculations we artificially remove this double layer once it is thin enough, thus modeling rupture. If no rupture takes place, the drops always rebound, but if the film is ruptured the drops may coalesce permanently or coalesce temporarily and then split again.

14. SUBJECT TERMS

Drop dynamics; Front tracking; Finite difference technique; Navier-Stokes equation

15. NUMBER OF PAGES
50

16. PRICE CODE
A03

17. SECURITY CLASSIFICATION OF REPORT	18. SECURITY CLASSIFICATION OF THIS PAGE	19. SECURITY CLASSIFICATION OF ABSTRACT	20. LIMITATION OF ABSTRACT
Unclassified	Unclassified	Unclassified	